

# Equatorial Pacific pCO<sub>2</sub> Interannual Variability in CMIP6 Models

Suki Cheuk-Kiu Wong<sup>1</sup>, Galen A McKinley<sup>2</sup>, and Richard Seager<sup>3</sup>

<sup>1</sup>Lamont-Doherty Earth Observatory at Columbia University

<sup>2</sup>Columbia University and Lamont-Doherty Earth Observatory

<sup>3</sup>Lamont Doherty Earth Observatory of Columbia University

January 20, 2023

## Abstract

The El Niño-Southern Oscillation (ENSO) in the equatorial Pacific is the dominant mode of global air-sea CO<sub>2</sub> flux interannual variability (IAV). Air-sea CO<sub>2</sub> fluxes are driven by the difference between atmospheric and surface ocean pCO<sub>2</sub>, with variability of the latter driving flux variability. Previous studies found that models in Coupled Model Intercomparison Project Phase 5 (CMIP5) failed to reproduce the observed ENSO-related pattern of CO<sub>2</sub> fluxes and had weak pCO<sub>2</sub> IAV, which were explained by both weak upwelling IAV and weak mean vertical DIC gradients. We assess whether the latest generation of CMIP6 models can reproduce equatorial Pacific pCO<sub>2</sub> IAV by validating models against observations-based data products. We decompose pCO<sub>2</sub> IAV into thermally and non-thermally driven anomalies to examine the balance between these competing anomalies, which explain the total pCO<sub>2</sub> IAV. The majority of CMIP6 models underestimate pCO<sub>2</sub> IAV, while they overestimate SST IAV. Thermal and non-thermal pCO<sub>2</sub> anomalies are not appropriately balanced in models, such that the resulting pCO<sub>2</sub> IAV is too weak. We compare the relative strengths of the vertical transport of temperature and DIC and evaluate their contributions to thermal and non-thermal pCO<sub>2</sub> anomalies. Model-to-observations-based product comparisons reveal that modeled mean vertical DIC gradients are biased weak relative to their mean vertical temperature gradients, but upwelling acting on these gradients is insufficient to explain the relative magnitudes of thermal and non-thermal pCO<sub>2</sub> anomalies.

# Equatorial Pacific pCO<sub>2</sub> Interannual Variability in CMIP6 Models

Suki C. K. Wong<sup>1</sup>, Galen A. McKinley<sup>1</sup>, Richard Seager<sup>1</sup>

<sup>1</sup>Lamont-Doherty Earth Observatory, Columbia University, Palisades, New York

## Key Points:

- The majority of models underestimate pCO<sub>2</sub> IAV, while they overestimate SST IAV
- Competing thermal and non-thermal pCO<sub>2</sub> components are not appropriately balanced in models, which results in weak total pCO<sub>2</sub> IAV
- Vertical DIC gradients are biased weak more than temperature gradients, but this alone doesn't explain the relative sizes of pCO<sub>2</sub> components

---

Corresponding author: Suki Wong, [suki.wong@columbia.edu](mailto:suki.wong@columbia.edu)

## Abstract

The El Niño-Southern Oscillation (ENSO) in the equatorial Pacific is the dominant mode of global air-sea CO<sub>2</sub> flux interannual variability (IAV). Air-sea CO<sub>2</sub> fluxes are driven by the difference between atmospheric and surface ocean pCO<sub>2</sub>, with variability of the latter driving flux variability. Previous studies found that models in Coupled Model Intercomparison Project Phase 5 (CMIP5) failed to reproduce the observed ENSO-related pattern of CO<sub>2</sub> fluxes and had weak pCO<sub>2</sub> IAV, which were explained by both weak upwelling IAV and weak mean vertical DIC gradients. We assess whether the latest generation of CMIP6 models can reproduce equatorial Pacific pCO<sub>2</sub> IAV by validating models against observations-based data products. We decompose pCO<sub>2</sub> IAV into thermally and non-thermally driven anomalies to examine the balance between these competing anomalies, which explain the total pCO<sub>2</sub> IAV. The majority of CMIP6 models underestimate pCO<sub>2</sub> IAV, while they overestimate SST IAV. Thermal and non-thermal pCO<sub>2</sub> anomalies are not appropriately balanced in models, such that the resulting pCO<sub>2</sub> IAV is too weak. We compare the relative strengths of the vertical transport of temperature and DIC and evaluate their contributions to thermal and non-thermal pCO<sub>2</sub> anomalies. Model-to-observations-based product comparisons reveal that modeled mean vertical DIC gradients are biased weak relative to their mean vertical temperature gradients, but upwelling acting on these gradients is insufficient to explain the relative magnitudes of thermal and non-thermal pCO<sub>2</sub> anomalies.

## Plain Language Summary

To date, the global ocean has been responsible for absorbing over a third of carbon dioxide (CO<sub>2</sub>) emissions, slowing down the growth of atmospheric CO<sub>2</sub> levels which drives global warming. Of interest is the equatorial Pacific Ocean, which is the largest oceanic source of CO<sub>2</sub> to the atmosphere with large fluctuations that are apparent in the record of global atmospheric CO<sub>2</sub>. To study the ocean's ability to absorb future CO<sub>2</sub> emissions, we need models of the Earth system that can accurately capture fluctuations in the equatorial Pacific. In this paper, we assess surface ocean CO<sub>2</sub> fluctuations in the equatorial Pacific in the latest generation of models and we examine their deviations from observations. Compared to observations, models underestimate surface ocean CO<sub>2</sub> fluctuations as a result of excessive cancellation between competing drivers of CO<sub>2</sub> change. We find that the vertical gradient of carbon in models is too weak, which through ocean circulation, would contribute to weak surface CO<sub>2</sub> fluctuations. However, this does not fully account for underestimations in surface CO<sub>2</sub> fluctuations. Other processes have a significant role in excessively canceling surface CO<sub>2</sub> concentrations and requires further research.

## 1 Introduction

Carbon dioxide (CO<sub>2</sub>) in the atmosphere is the main driver of anthropogenic radiative forcing via the greenhouse effect. Natural sinks in the ocean and land are damping the atmospheric CO<sub>2</sub> growth rate. The latest assessment of the global carbon budget averaged over recent decades (1960-2020) estimates the airborne fraction of atmospheric CO<sub>2</sub> emissions to be about 45%, with the remainder of emissions partitioned among the ocean (25%) and land (30%) (Friedlingstein et al., 2022). However, uncertainties in quantifying aspects of the global carbon cycle result in an imbalance in the carbon budget, which is largely attributed to errors in land and ocean sink estimates (Friedlingstein et al., 2022). Constraining ocean interannual variability (IAV) will help to reduce uncertainty in land IAV.

The equatorial Pacific is the largest natural oceanic source of CO<sub>2</sub> to the atmosphere (Takahashi et al., 2009), as a result of wind-driven upwelling in the region; upwelling brings cool waters that are rich in dissolved inorganic carbon (DIC) to the surface, which in-

creases the partial pressure of  $\text{CO}_2$  in the surface ocean ( $\text{pCO}_2$ ).  $\text{CO}_2$  outgassing IAV in the equatorial Pacific is dominated by the El Niño-Southern Oscillation (ENSO), and is the dominant mode of global ocean sink IAV (Rödenbeck et al., 2014). ENSO mechanisms of air-sea  $\text{CO}_2$  flux ( $\text{FCO}_2$ ) variability are well understood. During an ENSO warm phase (El Niño), slackening trade winds over the equator reduces upwelling and brings about warm sea surface temperature (SST) anomalies (Bjerknes, 1966). Warm SST anomalies increase  $\text{pCO}_2$  via reduced  $\text{CO}_2$  solubility. However, it is the reduction in surface DIC due to reduced upwelling that dominates the  $\text{CO}_2$  response (reduced  $\text{CO}_2$  outgassing) during an El Niño (McKinley et al., 2004). During an ENSO cold phase (La Niña), the opposite happens and  $\text{CO}_2$  outgassing is enhanced.

In Coupled Model Intercomparison Project Phase 5 (CMIP5), atmosphere-ocean global climate models were coupled with biogeochemical processes for the first time in CMIP history, allowing for carbon cycling in models (Taylor et al., 2012; Emori et al., 2016). Studies have reported biases in simulated equatorial Pacific  $\text{pCO}_2$  and  $\text{FCO}_2$  IAV in CMIP5 models, where weak surface DIC variability was found to be a source of bias in some models (Dong et al., 2017; Jin et al., 2019). Given ongoing climate change, there is a need for Earth System Models (ESMs) to make accurate climate projections. The latest generation of ESMs from CMIP6 have demonstrated progress in representing the mean state of ocean biogeochemistry (Séférian et al., 2020). However, as in CMIP5, weak  $\text{FCO}_2$  IAV were also found in CMIP6 (Vaithinada Ayar et al., 2022). Identifying sources of model biases in  $\text{FCO}_2$  IAV for the contemporary period, where some data constraints exist, is a first step towards model improvements.

Here, we assess equatorial Pacific  $\text{pCO}_2$  IAV in 18 CMIP6 models over recent decades, comparing amplitudes and spatial patterns of variability against state-of-the-art observations-based  $\text{pCO}_2$  products that span over five decades. We also compare the covariability of ENSO-related variables, such as SSTs, vertical velocity at 50m ( $w_{50}$ ), and thermocline depths with  $\text{pCO}_2$  anomalies across the CMIP6 subset through lagged correlations. To understand biases in  $\text{pCO}_2$  IAV, we decompose  $\text{pCO}_2$  IAV into thermally (SST) and non-thermally (DIC, alkalinity and salinity) driven components. Imbalances between these competing components provide insight on biases in the total  $\text{pCO}_2$  IAV.

In the equatorial Pacific, surface DIC variability dominates  $\text{pCO}_2$  variability (Doney et al., 2009). Though there are several processes that drive DIC variability ( $\text{FCO}_2$ , freshwater fluxes, biology, vertical and horizontal transport), studies show that variability in the vertical transport of DIC is important to the overall budget of  $\text{pCO}_2$  variability in the equatorial Pacific Ocean (Liao et al., 2020). Including temperature-driven  $\text{pCO}_2$  variability, Liao et al. (2020) showed that the vertical transport term contributed the largest amount in their full mixed-layer  $\text{pCO}_2$  budget decomposition (accounting for about 40% of the  $\text{pCO}_2$  response;  $\text{FCO}_2 \sim 20\%$ ; biology  $\sim 18\%$ ; freshwater fluxes  $\sim 11\%$ ; horizontal transport  $\sim 10\%$ ; thermal and residual  $< 1\%$ ). This demonstrated importance of the vertical transport of DIC in the equatorial Pacific motivates our investigation of its variability in CMIP6. There is also reason to believe that models are biased in mean vertical gradients (Li & Xie, 2012; Farneti et al., 2022), which through upwelling, could contribute to biases in surface DIC variability.

Our objectives are as follows: 1) compare equatorial Pacific  $\text{pCO}_2$  IAV in CMIP6 models against observations-based data products, 2) understand why models underestimate  $\text{pCO}_2$  IAV, and 3) identify sources of bias in the vertical transport of DIC in models. Given biases in mean vertical gradients of DIC and temperature, we quantify the degree to which upwelling anomalies (acting on biased gradients) contribute to the relative magnitudes of non-thermal and thermal  $\text{pCO}_2$  IAV, respectively. Such assessment is necessary to ground work on how future changes in the variability and mean state of the tropical Pacific atmosphere-ocean system will also impact variability and shifts in air-sea  $\text{CO}_2$  fluxes, with potential climate impact.



**Table 1.** The CMIP6 models in this assessment and their references. For information about the ensemble members, see Table S1. Models in bold have a correct sign correlation between  $p\text{CO}_2$  and vertical velocity and are assessed in all parts of this study.

Models	Reference
ACCESS-ESM1-5	(Ziehn et al., 2019)
<b>CanESM5</b>	(Swart et al., 2019b)
CanESM5-CanOE	(Swart et al., 2019a)
<b>CESM2</b>	(Danabasoglu, 2019b)
<b>CESM2-FV2</b>	(Danabasoglu, 2019a)
<b>CESM2-WACCM</b>	(Danabasoglu, 2019d)
<b>CESM2-WACCM-FV2</b>	(Danabasoglu, 2019c)
<b>CNRM-ESM2-1</b>	(Seferian, 2018)
<b>GFDL-CM4</b>	(Guo et al., 2018)
IPSL-CM6A-LR	(Boucher et al., 2021)
<b>MIROC-ES2L</b>	(Hajima et al., 2019)
<b>MRI-ESM2-0</b>	(Yukimoto et al., 2019)
MPI-ESM1-2-LR	(Wieners et al., 2019)
MPI-ESM1-2-HR	(Jungclaus et al., 2019)
MPI-ESM-1-2-HAM	(Neubauer et al., 2019)
<b>NorESM2-LM</b>	(Seland et al., 2019)
<b>NorESM2-MM</b>	(Bentsen et al., 2019)
<b>UKESM1-0-LL</b>	(Byun, 2020)

## 2 Models, Data and Methods

### 2.1 Models

Outputs from historical simulations (1959-2014) from 18 CMIP6 models (Table 1) are from the Pangeo cloud (<http://pangeo.io>), which were originally downloaded from the Earth System Grid Federation’s online archives (<http://esgf-node.llnl.gov/projects/cmip6>). We apply a data pre-processing Python tool to clean and unify data inconsistencies before any analysis (Busecke & Abernathy, 2020). We assess 18 models which have monthly  $p\text{CO}_2$ ,  $\text{FCO}_2$ , SST, near-surface wind speeds measured at 10m ( $u_{10}$ ), ocean temperatures (T),  $w_{50}$  and DIC data available. Vertical velocities are calculated using the three-dimensional continuity equation for models that only have horizontal circulation data. For analyses that involve multiple ensemble members, ensemble members are chosen only if they have outputs for all the variables named above. This ensures that the internal variability, unique to each run of a model (an ensemble member), is conserved across all output variables from a single run. For a list of the members that we use for each model, see Table S1.

### 2.2 Observations-based Data Products

We use five out of the six available monthly gridded observations-based  $p\text{CO}_2$  products from SeaFlux (Fay et al., 2021) for  $\text{FCO}_2$  and surface ocean  $p\text{CO}_2$  estimates. These five products include JENA-MLS, MPI-SOMFFN, CMEMS-FFN, JMA-MLR and CSIR-ML6. We exclude a sixth product (NIES-FFNN) from our assessment as it was not able to recreate ENSO variability in  $p\text{CO}_2$ , such as the strong 1997-98 El Niño event seen in the other products. For  $u_{10}$  data, we also use the three wind reanalysis products (CCMPv2, JRA55 and ERA5), used in SeaFlux to estimate fluxes.

DIC and total alkalinity (Alk) climatologies are from GLODAPv2 (Lauvset et al., 2021). GLODAPv2 is a mapped three-dimensional climatological data product of inorganic and carbon-related ocean variables. Observations of DIC and Alk are distributed in time too scarcely to allow determination of its time variation, so in GLODAPv2, the data have been averaged into a DIC climatology estimate. Monthly estimates of SST, ocean circulation and ocean temperature (1959-2014) are from a reanalysis product, ORAS5 of the European Center for Medium Range Weather Forecasts (Zuo et al., 2019). Unlike DIC and Alk, time variations can be resolved for SST, ocean circulation and ocean temperature variables in observations-based data products. We calculate vertical velocity using zonal and meridional ocean circulation data from ORAS5 via the vertical integration of the continuity equation. SST observations from another dataset, HadISST (1959-2014; Rayner et al. (2003)), are a secondary source for SST comparisons against models.

### 2.3 Methods

Model outputs are regridded to the same  $1^\circ \times 1^\circ$  longitude-latitude grid before any analysis. We define a region of the equatorial Pacific ( $5^\circ\text{N}$ - $5^\circ\text{S}$ ) between  $180^\circ\text{E}$  and  $270^\circ\text{E}$ , which encompasses the Niño 3 and 3.4 regions, extending 10 degrees west of Niño 3.4, and refer to it as the Tropical Pacific Index (TPI) region. The Niño 3 and 3.4 regions are typically used to study the nature of ENSO variability over the equatorial Pacific Ocean, but here, the broader TPI region was chosen such that any longitudinal differences in the ENSO centers of action in models would be captured.

To compare relative amplitudes of IAV across models and other datasets, we use one standard deviation ( $\sigma$ ) of detrended and deseasonalized monthly anomalies. Modeled  $\text{FCO}_2$ ,  $\text{pCO}_2$  and  $u_{10}$  IAV are compared against SeaFlux IAV. Note that historical simulations in CMIP6 models generate their own internal climate variability, and will not replicate the timings of historical events unless they are externally forced. Thus, when comparing SeaFlux IAV to model IAV, the temporal evolution is not expected to match. When calculating and comparing multi-year means between CMIP6 models and SeaFlux, data from the same time frame (1990 to 2014) are compared. This is done since multi-year means are sensitive to anthropogenic trends in  $\text{CO}_2$ ; the ocean sink is changing over time in both observations-based data products and historical simulations, such that multi-year means are sensitive to the time frame over which the average is taken. The 1990-2014 time frame is chosen for multi-year means, because temporal coverage begins in 1990 for SeaFlux, and 2014 is the end year for CMIP6 historical simulations. Climatological monthly means taken over the study period are subtracted from monthly timeseries data to obtain deseasonalized monthly anomalies, and then, the data are detrended with the least squares method. In addition to model comparisons against SeaFlux, modeled SST IAV and vertical DIC gradients IAV are also compared against observations-based data products.

Spatial patterns of  $\text{pCO}_2$  IAV are compared and assessed by calculating its first empirical orthogonal function (EOF) after detrending and deseasonalizing. EOF analyses are done on individual ensemble members that retain full internal variability, and then averaged across ensemble members. The first principal components (PC1) and associated EOFs are all shown for the La Niña state, as determined with reference to the sign of the TPI SST index. Model performances in reproducing IAV are assessed using spatial correlation coefficients (SCC) between each model and observations-based  $\text{pCO}_2$  patterns of IAV.

In order to examine the mechanisms of  $\text{pCO}_2$  variability in models, local correlations between  $\text{pCO}_2$  and SST anomalies within the tropical Pacific are calculated. Areas of strong correlations indicate regions in models where upwelling dominates  $\text{pCO}_2$ , which is consistent with the dominant ENSO signal. Lagged temporal correlations be-

tween  $pCO_2$ , SST,  $w_{50}$  and thermocline depth ( $z_{\text{therm}}$ ) anomalies are also done to investigate the covariability of ENSO-related variables to  $pCO_2$  anomalies. We define the  $z_{\text{therm}}$  as the depth of the maximum vertical temperature gradient. Time lags between variables are based on the lags seen in the observations-based data products:  $pCO_2$  and SST are concurrently correlated, while  $w_{50}$  and  $z_{\text{therm}}$  anomalies lead  $pCO_2$  by up to 3 months. Three-month running means of  $w_{50}$  and  $z_{\text{therm}}$  anomalies are taken before correlating them to the  $pCO_2$  of the fourth month (e.g., the January-to-March mean of  $w_{50}$  anomalies are correlated to April's  $pCO_2$  anomaly).  $pCO_2$  is long-lived in the ocean, such that the influence of  $w_{50}$  and  $z_{\text{therm}}$  variability on local  $pCO_2$  advects west due to mean currents during the three months of lag. To account for some of the westward advection of  $pCO_2$  during the lag period,  $w_{50}$  and  $z_{\text{therm}}$  anomalies are calculated over a region  $20^\circ$  east of the TPI box region before correlating with  $pCO_2$  anomalies over the TPI box region.

## 2.4 Thermal and Non-thermal $pCO_2$ IAV

Variability in DIC, alkalinity (Alk) and salinity (S) are the non-thermal drivers of  $pCO_2$  variability, while SST variability is the thermal driver. Thermal effects on  $pCO_2$  typically oppose and dampen the non-thermal effects with ENSO (Sutton et al., 2014): for example, a reduction in upwelling brings less DIC to the surface which decreases surface  $pCO_2$ ; simultaneously, the warmer SST anomalies, as a result of weakened upwelling, drives surface  $pCO_2$  up via reduced solubility. We separate the non-thermally driven  $pCO_2$  ( $pCO_{2,nonT}$ ) from the thermally-driven counterpart ( $pCO_{2,T}$ ) in order to explain modeled  $pCO_2$  IAV. For  $pCO_{2,nonT}$ , temperature effects are removed by normalizing  $pCO_2$  outputs to a long-term mean SST (Takahashi et al., 2002), following an empirical formulation determined by Takahashi et al. (1993):

$$pCO_{2,nonT} = pCO_2 \times e^{0.0423 \cdot (\overline{SST} - SST)}, \quad (1)$$

where  $\overline{SST}$  is the multiyear mean of SST over time. The thermally driven component,  $pCO_{2,T}$ , is computed using the following equation (Takahashi et al., 2002):

$$pCO_{2,T} = \overline{pCO_2} \times e^{0.0423 \cdot (SST - \overline{SST})}, \quad (2)$$

where  $\overline{pCO_2}$  is the multiyear mean of  $pCO_2$  during 1990-2014.

## 2.5 Vertical Transport of DIC

Temporal changes in  $pCO_2$  are a function of temporal changes in DIC, Alk, S and T, and can be expressed as the following linearly decomposed time derivative (Takahashi et al., 1993; Le Quéré et al., 2000; Liao et al., 2020):

$$\partial_t pCO_2 = \underbrace{\frac{\partial pCO_2}{\partial DIC} \partial_t DIC + \frac{\partial pCO_2}{\partial Alk} \partial_t Alk + \frac{\partial pCO_2}{\partial S} \partial_t S}_{\text{non-thermal}} + \underbrace{\frac{\partial pCO_2}{\partial T} \partial_t T}_{\text{thermal}}, \quad (3)$$

where we use the notation  $\partial_t$  to denote a partial derivative with respect to time. Temporal changes in DIC, Alk and S drive  $pCO_{2,nonT}$ , while temporal changes in SST drive  $pCO_{2,T}$ .

In the tropical Pacific, DIC variability has been found to be the dominant driver of  $pCO_2$  variability, compared to Alk, S and T drivers (Doney et al., 2009; Le Quéré et al., 2000). Note that Liao et al. (2020) found that in some cases, alkalinity-driven effects on  $pCO_2$  can exceed DIC-driven effects, though DIC effects generally dominate in the equatorial Pacific. Other model studies confirm that DIC is the dominant term in the region (Jin et al., 2019; Long et al., 2013).

The time tendency of surface DIC ( $\partial_t \text{DIC}$ ) is controlled by several processes including horizontal and vertical ocean transport,  $\text{FCO}_2$ , biological processes and freshwater fluxes:

$$\partial_t \text{DIC} \approx \partial_t \text{DIC}_H + \partial_t \text{DIC}_V + \partial_t \text{DIC}_{\text{FCO}_2} + \partial_t \text{DIC}_{\text{Bio}} + \partial_t \text{DIC}_{\text{FW}} \quad (4)$$

In this study, we assess only the variability in vertical transport of DIC ( $\partial_t \text{DIC}_V$ ). Liao et al. (2020) showed that though other processes are non-negligible, vertical transport contributed the largest effect on  $\text{pCO}_2$  change. They also showed that the other processes are sensitive to changes in vertical transport: an increase in upwelling (increased surface DIC) drives an air-sea flux response, which damps surface DIC; upwelled nutrient-rich waters increase biological activity causing an increased uptake of DIC, which again damps surface DIC; and the horizontal transport of increased surface DIC results in a diverging transport, also damping.

In order to quantify the contribution of the vertical transport of DIC ( $\partial_t \text{DIC}_V$ ) to  $\text{pCO}_{2, \text{nonT}}$  variability ( $\partial_t \text{pCO}_{2, \text{nonT}}$ ), we evaluate the former in the same units as the latter - in units of the time tendency of  $\text{pCO}_2$  ( $\mu\text{atm s}^{-1}$ ) - and write  $\partial_t \text{DIC}_V$  as  $w_{50} \partial_z \text{DIC}$ . Using coefficients from Equation 3, we can get both terms into the same units:

$$\frac{\partial \text{pCO}_2}{\partial \text{DIC}} w_{50} \partial_z \text{DIC} \quad [\text{units : } \mu\text{atm s}^{-1}] \quad (5)$$

$$\partial_t \text{pCO}_{2, \text{nonT}} \quad [\text{units : } \mu\text{atm s}^{-1}] \quad (6)$$

The coefficients used for the  $\text{pCO}_2$  dependence on DIC are approximated as follows (Lovenduski et al., 2007):

$$\frac{\partial \text{pCO}_2}{\partial \text{DIC}} \approx \frac{\overline{\text{pCO}_2}}{\overline{\text{DIC}}} \cdot \frac{3 \times \overline{\text{Alk}} \times \overline{\text{DIC}} - 2 \times \overline{\text{DIC}}^2}{(2 \times \overline{\text{DIC}} - \overline{\text{Alk}})(\overline{\text{Alk}} - \overline{\text{DIC}})}, \quad (7)$$

which can be expressed more simply as:

$$\frac{\partial \text{pCO}_2}{\partial \text{DIC}} \approx \frac{\overline{\text{pCO}_2}}{\overline{\text{DIC}}} \cdot \gamma_{\text{DIC}}, \quad (8)$$

where  $\gamma_{\text{DIC}}$  is the buffer factor (Sarmiento & Gruber, 2006).

## 2.6 Reynolds' Decomposition

Using Reynolds' decomposition, we can separate the mean and the time-varying component:

$$w_{50} = \overline{w_{50}} + w'_{50}, \text{ and} \quad (9)$$

$$\partial_z \text{DIC} = \partial_z \overline{\text{DIC}} + \partial_z \text{DIC}', \quad (10)$$

where primes denote detrended monthly anomalies and overbars denote long-term means. We can decompose the time varying vertical transport of DIC,  $\gamma_{\text{DIC}}(w_{50} \partial_z \text{DIC})$ , into three Reynolds' terms:

$$\gamma_{\text{DIC}}(w_{50} \partial_z \text{DIC})' = \gamma_{\text{DIC}}(\overline{w_{50}} \partial_z \text{DIC}' + w'_{50} \partial_z \overline{\text{DIC}} + w'_{50} \partial_z \text{DIC}') \quad (11)$$

For models, we can compute all three Reynold's terms. However, for observations-based data products, we can only compute the second Reynold's term ( $w'_{50} \partial_z \overline{\text{DIC}}$ ) since gridded DIC data are only available as a climatology. Therefore, only the second Reynolds' terms are compared.

### 3 Results

A large region of  $\text{FCO}_2$  outgassing can be seen in the equatorial Pacific Ocean, with the highest, (positive, red) values being in the eastern region in SeaFlux (Figure 1a). Comparing mean fluxes, three models (MRI-ESM2-0, MPI-ESM-1-2-HAM and UKESM1-0-LL) are shown in Figure 1b. The models have similar patterns to SeaFlux to the first order, with a basin-wide outgassing feature seen over the equatorial Pacific region, and the largest values lying in the eastern region. Similar maps for all the CMIP6 models are available in Figure S1. Model mean fluxes in the equatorial Pacific are typically weaker than SeaFlux, with the exception of UKESM1-0-LL which has a mean magnitude closer to SeaFlux (the CESM2 family of models also have comparable mean  $\text{FCO}_2$  values, Figure S1). The mean outgassing in the equatorial region is noticeably weaker in MRI-ESM2-0 than the other models, and the MPI models show a narrow band of near-zero flux at the equator in the middle of the broader equatorial outgassing pattern.

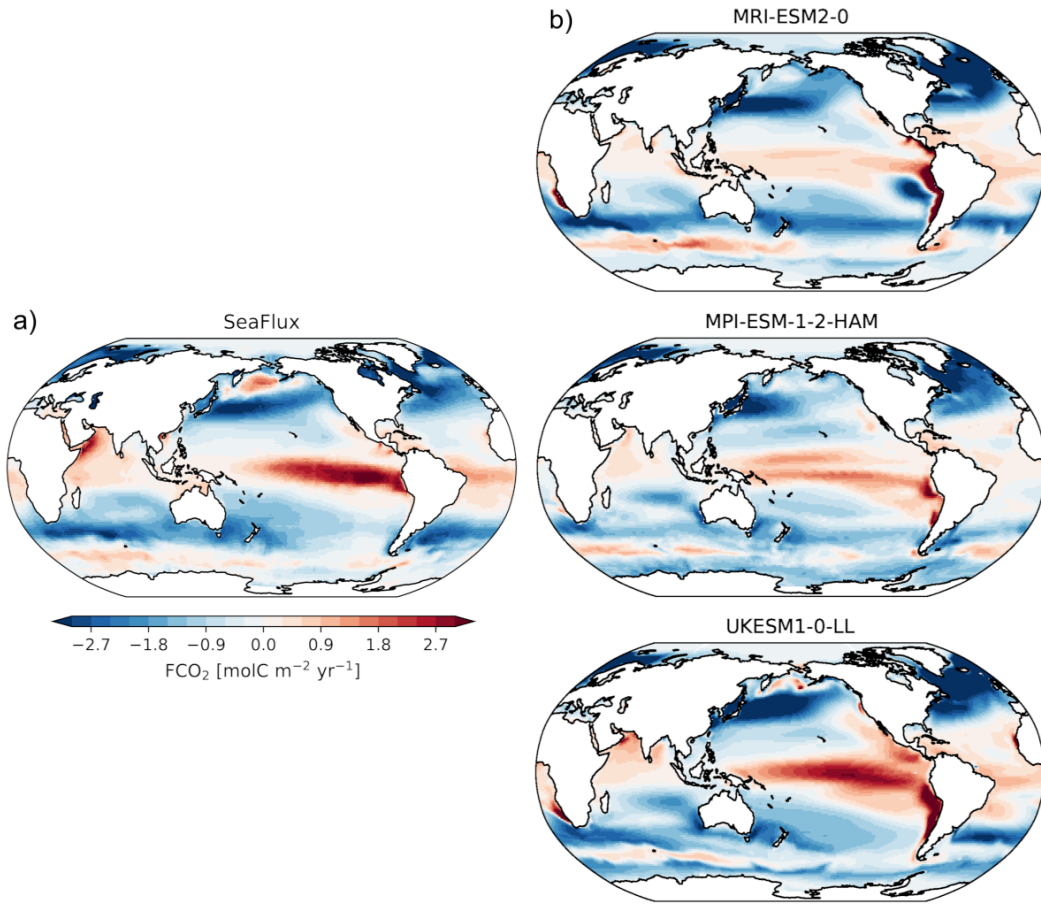


**Figure 1.** Multiyear mean maps of air-sea  $\text{CO}_2$  flux ( $\text{FCO}_2$  units:  $\text{mol C m}^{-2} \text{ yr}^{-1}$ ) taken over 1990-2014 for: a) the SeaFlux ensemble-average, and b) three CMIP6 models (one member was chosen per model): MRI-ESM2-0, MPI-ESM-1-2-HAM and UKESM1-0-LL. Positive values (red) represent fluxes from the ocean to the atmosphere. Similar maps for the remaining CMIP6 models are in Figure S1.

### 3.1 pCO<sub>2</sub> Interannual Variability and Multiyear Means

The outgassing of CO<sub>2</sub> in the equatorial Pacific Ocean (Figure 1) is modulated by ENSO variability, which dominates the variability of global oceanic FCO<sub>2</sub> (Landschützer et al., 2016; McKinley et al., 2017; McKinley et al., 2004). Amplitudes of FCO<sub>2</sub> IAV ( $\sigma_{\text{FCO}_2}$ ) in the TPI region in CMIP6 differ from SeaFlux observations-based data products (Figure 2a). The majority of CMIP6 models underestimate FCO<sub>2</sub> IAV relative to SeaFlux over the TPI region with the exception of CESM2, CESM2-FV2, CNRM-ESM2-1 and MIROC-ES2L, which have members with FCO<sub>2</sub> IAV amplitudes that overlap with SeaFlux.

FCO<sub>2</sub> is a function of surface ocean and atmospheric pCO<sub>2</sub>, and in the parameterization used in the models and data products, has a quadratic relationship to near-surface wind speeds,  $u_{10}$  (Wanninkhof, 2014). To investigate the underestimation of FCO<sub>2</sub> seen in CMIP6, we assess their amplitudes of pCO<sub>2</sub> and  $u_{10}$  IAV:  $\sigma_{\text{pCO}_2}$  and  $\sigma_{u'_{10}}$ , respectively (see Figure 2b, c). Similar to the FCO<sub>2</sub> IAV estimates, the majority of CMIP6 models underestimate pCO<sub>2</sub> IAV relative to SeaFlux. Meanwhile,  $u_{10}$  IAV is overestimated across the majority of models, with the exception of the CanESM5 models, the MPI models, and some smaller underestimation discrepancies from the GFDL-CM4 and MRI-ESM2-0 models, relative to three wind reanalysis data products. The underestimation in modeled pCO<sub>2</sub> IAV appears to be compensated by the overestimation in  $u_{10}$  IAV. In the MPI models, pCO<sub>2</sub> IAV is within range of data products, but FCO<sub>2</sub> is low due to low  $u_{10}$  IAV.

ENSO-driven variability has a concomitant effect on SST variability in the equatorial Pacific via the upwelling of cool waters. Figure 2d shows that the majority of CMIP6 models overestimate SST IAV in the TPI region, relative to ORAS5 and HadISST estimates. Models that underestimate pCO<sub>2</sub> IAV also overestimate SST IAV, with the exception of the CanESM5 models which underestimate both SST and pCO<sub>2</sub> IAV. Models also tend to overestimate  $u_{10}$  variance (Figures 2c, d). This is consistent with the coupling of wind speeds and SST variability via the Bjerknes feedback, where they amplify each other's anomalies.

Multiyear mean maps of pCO<sub>2</sub>, averaged over 1990 to 2014, are plotted for SeaFlux and five of the CMIP6 models (Figure 3; Figure S2: all models). A spatial correlation coefficient (SCC) over the TPI region is calculated between each model and SeaFlux to quantify the model skill at reproducing the mean pCO<sub>2</sub> pattern. Note that a high SCC score does not indicate that the magnitude of the mean maps are similar. Generally, the majority of models produce the high pCO<sub>2</sub> equatorial structure seen in SeaFlux, with a third of models having an SCC score above 0.8 (Figure S2). The largest pCO<sub>2</sub> values are seen off coastal Peru and Panama in SeaFlux, with exaggerated coastal values seen in some of the models (ACCESS-ESM1-5, MRI-ESM2-0, and UKESM1-0-LL). Unlike SeaFlux, the high pCO<sub>2</sub> equatorial structure extends almost all the way across the basin in the majority of models, except for the NorESM2 models. Similar to the FCO<sub>2</sub> multiyear mean maps, the MPI models show mean pCO<sub>2</sub> structures that exhibit an equatorial band of low pCO<sub>2</sub> that splits up the general high pCO<sub>2</sub> structure seen in SeaFlux and the other models.

### 3.2 Spatial Patterns of pCO<sub>2</sub> IAV

The EOF1 of SeaFlux (Figure 4: top left) explains 41% of the total variance in pCO<sub>2</sub> IAV in the tropical Pacific, with a pattern that resembles that of ENSO variability of FCO<sub>2</sub> (McKinley et al., 2004; Resplandy et al., 2015). Its corresponding first principal component (PC1) is highly correlated with ORAS5 SST anomalies in the TPI region ( $r = -0.82$ , see Figure S3 for PC1 results), which indicates ENSO-driven variability in the tropical Pacific Ocean in the observations-based products.



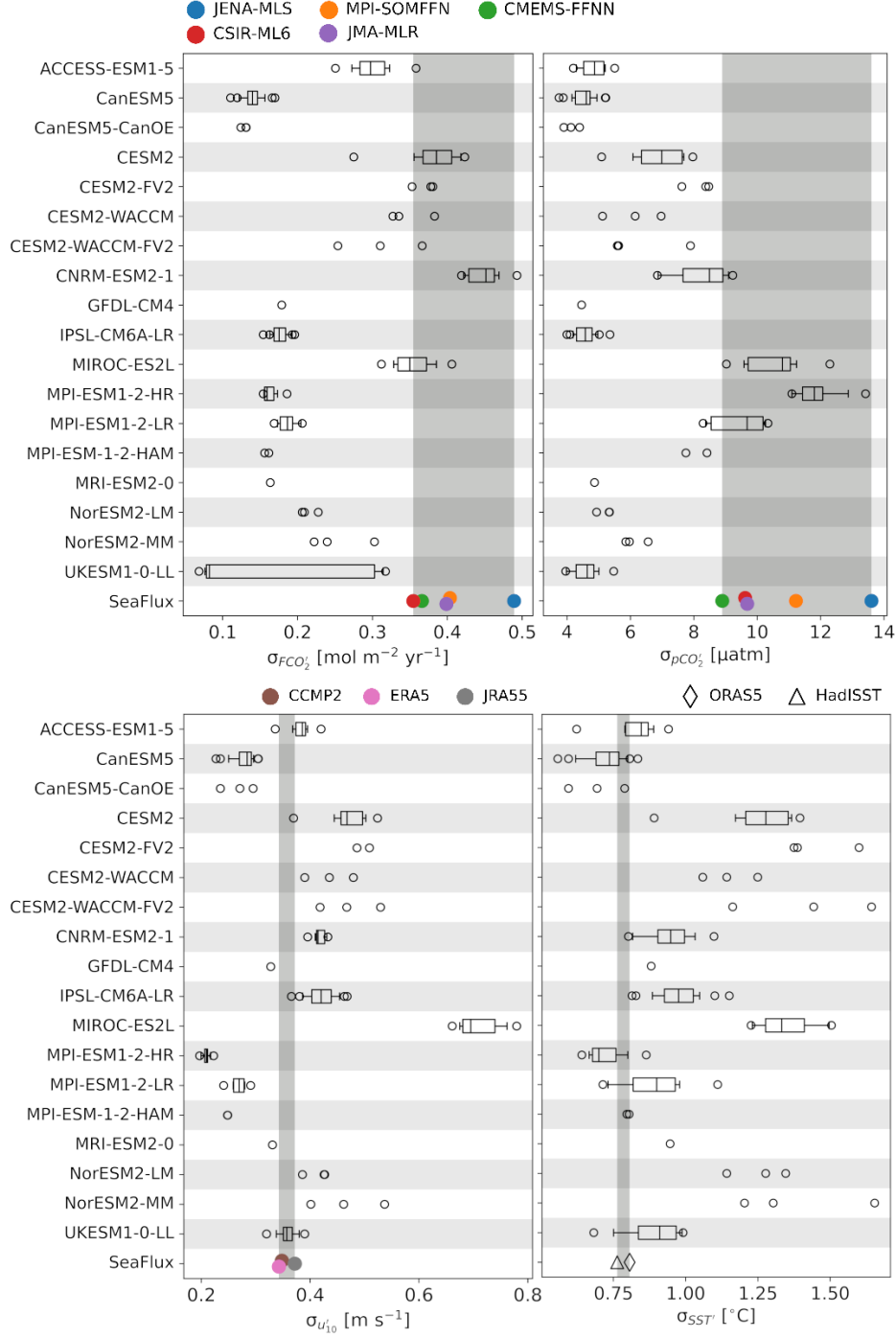


**Figure 2.** Comparison of IAV amplitudes in models (one standard deviation over the 1959–2014 period), and in observations-based data products (one standard deviation over the 1990–2014 period) in the Tropical Pacific Index (TPI) region (5°N–5°S, 180°E–270°E). Top-left:  $FCO_2$  IAV (units: mol C m<sup>-2</sup> yr<sup>-1</sup>); top-right:  $pCO_2$  IAV (units: μatm); bottom-left:  $u_{10}$  IAV (units: m s<sup>-1</sup>); bottom-right: SST IAV (units: °C). Boxplots represent the spread in IAV amplitudes within a model’s ensemble members. For models where fewer than three members were available, the spread is shown without a boxplot. observations-based data products are represented as the filled circles and the grey shaded regions indicate the range of IAV amplitudes within the observations-based data products.

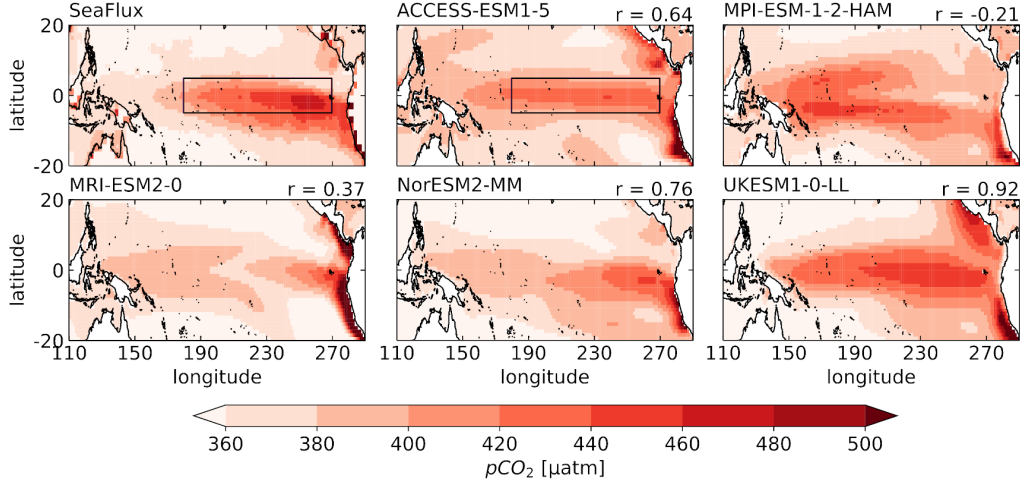


**Figure 3.** Tropical Pacific  $p\text{CO}_2$  multi-year means from 1990-2014 (units:  $\mu\text{atm}$ ) from the SeaFlux ensemble average (top left) and five CMIP6 models (other panels). Boxes in the SeaFlux and ACCESS-ESM1-5 panels mark the TPI region. The number ( $r$ ) on the top right of each model's map is the SCC between the model and SeaFlux in the TPI region. Model multi-year means are evaluated using a single ensemble member per model. Similar maps for all CMIP6 models are in Figure S2.

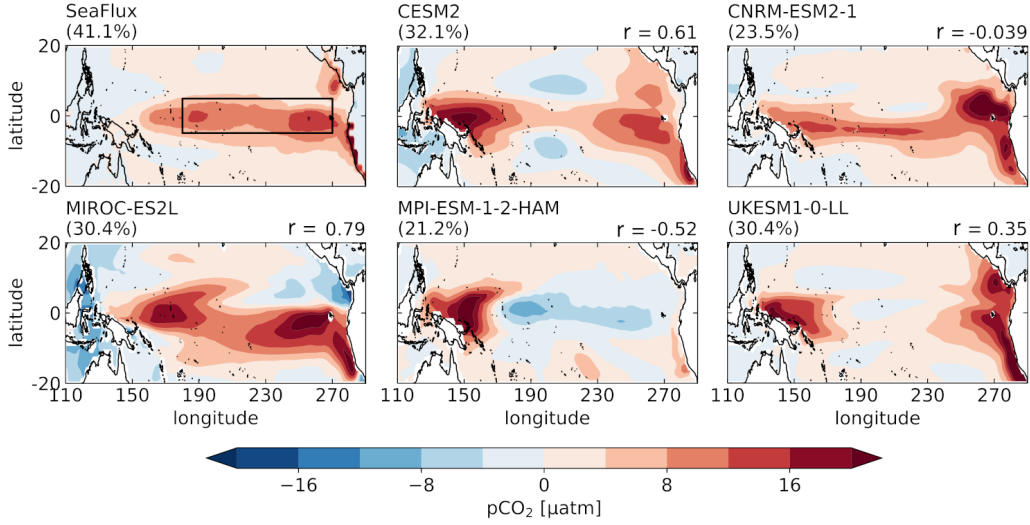


**Figure 4.** The first EOFs (units:  $\mu\text{atm}$ ) of detrended  $p\text{CO}_2$  anomalies in SeaFlux, averaged across the ensemble (top left), and 5 CMIP6 models (other panels). Model EOF patterns are calculated individually for each ensemble member before averaging over the ensemble. The percentage of the total variance in the tropical Pacific explained by EOF1 is given in parentheses above each panel. The number ( $r$ ) on the top right of each model's panel is the SCC over the TPI region between each model's EOF1 and SeaFlux's EOF1. The TPI region is shown by the box in the top-left panel. Similar maps for all CMIP6 models are in Figure S4. The corresponding PC1 timeseries are shown in Figure S3.



In CMIP6, few models have an EOF1 that resembles the ENSO pattern seen in SeaFlux (Figure 4; Figure S4: all models). Further, models that have a realistic spatial pattern have too little variance in the first EOF mode. For example, MIROC-ES2L has an EOF1 pattern most similar to SeaFlux ( $\text{SCC} = 0.79$ ), and explains 30% of the total  $\text{pCO}_2$  variance. The CESM2 models, CNRM-ESM2-1 and UKESM1-0-LL reveal almost two-centers of action – near the coastlines on either side of the tropical Pacific – for  $\text{pCO}_2$  variance. The weak correlation over the TPI region between SeaFlux and CNRM-ESM2-1 ( $\text{SCC} = -0.04$ ) is because the positive  $\text{pCO}_2$  variance in the model’s EOF1 is shifted slightly south of the equator. MPI models show a “negative” EOF1 pattern, revealing  $\text{pCO}_2$  variability that is opposite to what is expected from ENSO variability – i.e. the  $\text{pCO}_2$  and SST variability in its TPI region are positively correlated, in contrast to the negative correlation in SeaFlux.

Models that reproduce a realistic multiyear mean  $\text{pCO}_2$  map (Figure 3), with respect to SeaFlux, do not necessarily have a realistic ENSO pattern of variability (Figure 4). Nevertheless, the relationship between PC1 and TPI SST anomalies do tend to be strong, with a median correlation of  $r = -0.73$  (Figure S3). This is consistent with the ENSO signal where upwelling dominates  $\text{pCO}_2$  variability (Feely et al., 2006; Sutton et al., 2014).

Figure 5 compares maps of the local correlation coefficient between  $\text{pCO}_2$  and SST anomalies in models for the tropical Pacific. These correlations reveal the relative magnitude of  $\text{pCO}_{2,T}$  and  $\text{pCO}_{2,nonT}$  components of  $\text{pCO}_2$  variability, since the dominance of either component will result in a correlation coefficient that is either positive (thermally dominant) or negative (non-thermally dominant). The strong, negative correlation pattern (blue areas) over the equatorial Pacific, seen in SeaFlux (Figure 5: top left), indicates variability in upwelling of water that is both cool and DIC-rich with ENSO oscillations. Areas of positive correlations (red areas) indicate  $\text{pCO}_2$  variability that is thermally driven; warmer SSTs drive higher  $\text{pCO}_2$  levels. The negative  $\text{pCO}_2$ -SST relationship covers a broad region in SeaFlux that spans the basin, with the strongest negative correlations at the equator. Compared to SeaFlux, MIROC-ES2L shows a pattern that covers a similar longitudinal span, however, the intensity of the negative correlations are not as strong, and does not extend as far north. NorESM2-MM shows stronger correlations; however, its negative pattern does not cover the same longitudinal span as seen in SeaFlux. The lack of the negative  $\text{pCO}_2$ -to-SST extension to the west, common to most of the CMIP6 models, indicates that the ENSO- $\text{CO}_2$  co-variability lies more east in models than in SeaFlux. CNRM-ESM2-1, UKESM1-0-LL and ACCESS-ESM1-5 have a positive correlation zone within the Niño 3.4 region; CESM2 also has an anomalous positive correlation zone that lies more towards the east (Figure S5).

### 3.3 Thermal and Non-thermal $\text{pCO}_2$ IAV

For SeaFlux and the CMIP6 models, detrended  $\text{pCO}_2$  monthly anomalies decomposed into thermally ( $\text{pCO}_{2,T}$ ) and non-thermally ( $\text{pCO}_{2,nonT}$ ) driven anomalies (Equation 1, 2) indicate the relative magnitudes of thermally and non-thermally driven  $\text{pCO}_2$  variability (Figure 6: IPSL-CM6A-LR; S6: other models).

In SeaFlux,  $\text{pCO}_{2,T}$  ( $\text{pCO}_{2,nonT}$ ) anomalies are strongly, positively (negatively) correlated with SST anomalies, with correlation coefficients greater than 0.98. The total  $\text{pCO}_2$  anomaly (Figure 6, bold black line) is strongly negatively correlated ( $r = -0.92$ ) with TPI SST anomalies, due to the non-thermal component being dominant over the thermal component ( $\sigma_{\text{pCO}_{2,nonT}}' > \sigma_{\text{pCO}_{2,T}}'$ ).

In contrast, in IPSL-CM6A-LR (Figure 6: right), the non-thermal and thermal components have similar amplitudes but opposite sign ( $\sigma_{\text{pCO}_{2,nonT}}' \sim \sigma_{\text{pCO}_{2,T}}'$ ). This results in the total  $\text{pCO}_2$  anomaly having almost no correlation ( $r = -0.03$ ) with SST anomalies.  $\text{pCO}_{2,T}$  variability almost completely counteracts  $\text{pCO}_{2,nonT}$  variability, resulting

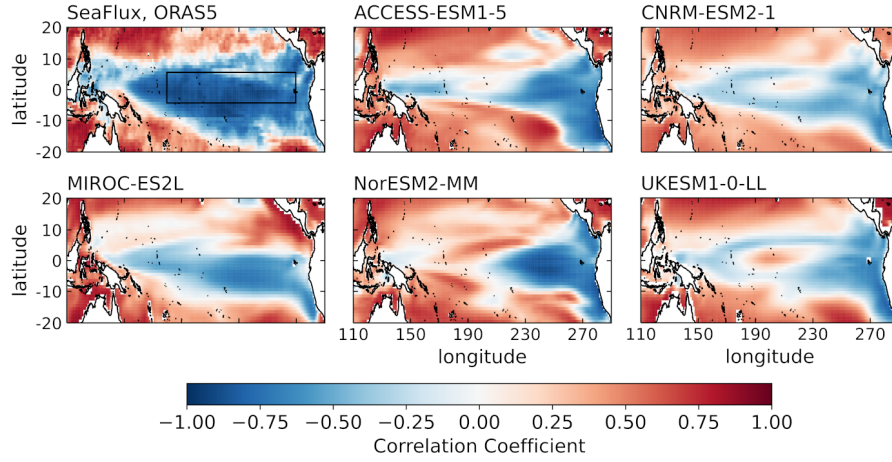


**Figure 5.** Correlation maps of detrended,  $p\text{CO}_2$  and SST monthly anomalies over the tropical Pacific region. Time periods used: 1990-2014 for SeaFlux and ORAS5 (top-left), and 1959-2014 for models (other panels). Model correlation maps were calculated individually for each ensemble member before averaging over the ensemble. For the observations-based map, the mean across SeaFlux  $p\text{CO}_2$  products was first taken before correlating with ORAS5 SSTs. Maps for all models are in Figure S5

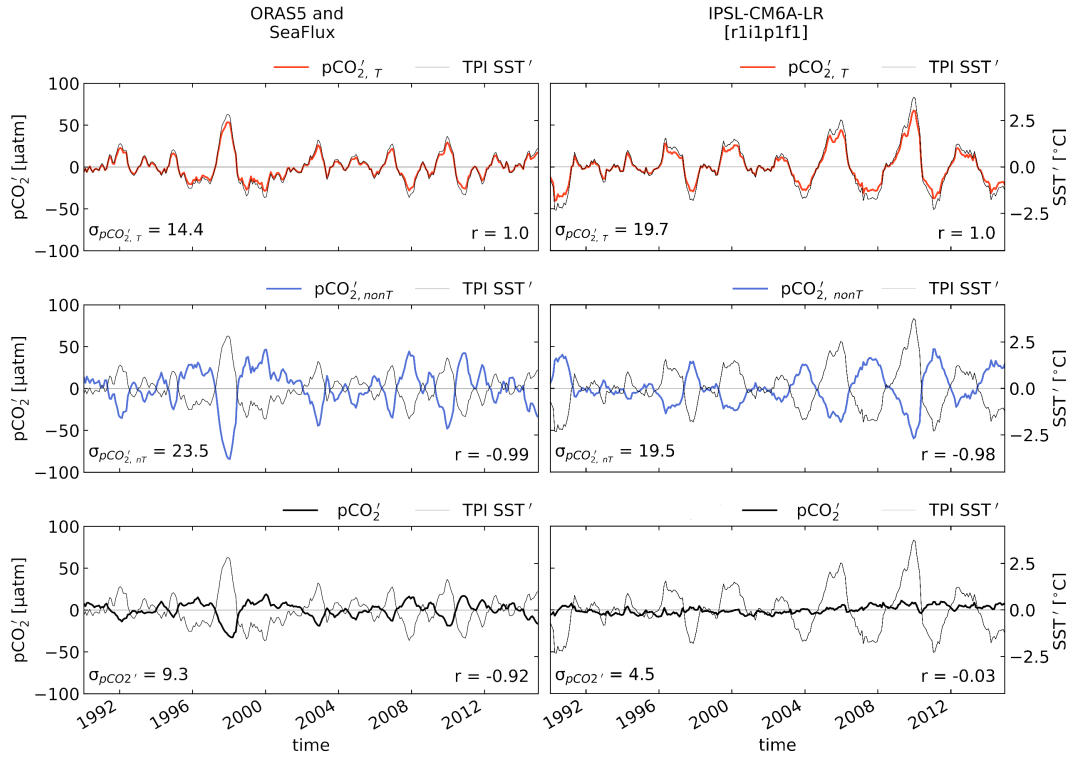


**Figure 6.** Timeseries of thermal, non-thermal and total  $p\text{CO}_2$  anomalies from an ensemble average of the SeaFlux products (left) and from a single member of IPSL-CM6A-LR (right); (top, red)  $p\text{CO}_{2,T}$  anomalies; (middle, blue)  $p\text{CO}_{2,nonT}$  anomalies; (bottom, black) net  $p\text{CO}_2$  anomalies (units:  $\mu\text{atm}$ ). All panels are overlaid with the TPI region's SST anomalies (units:  $^{\circ}\text{C}$ ; the SST y-axis is located on the right side of each panel). The bottom-left number in each panel is the IAV amplitude ( $\sigma$ ) of each timeseries, and the bottom-right number is the correlation coefficient ( $r$ ) of the  $p\text{CO}_2$  anomalies with the SST anomalies.

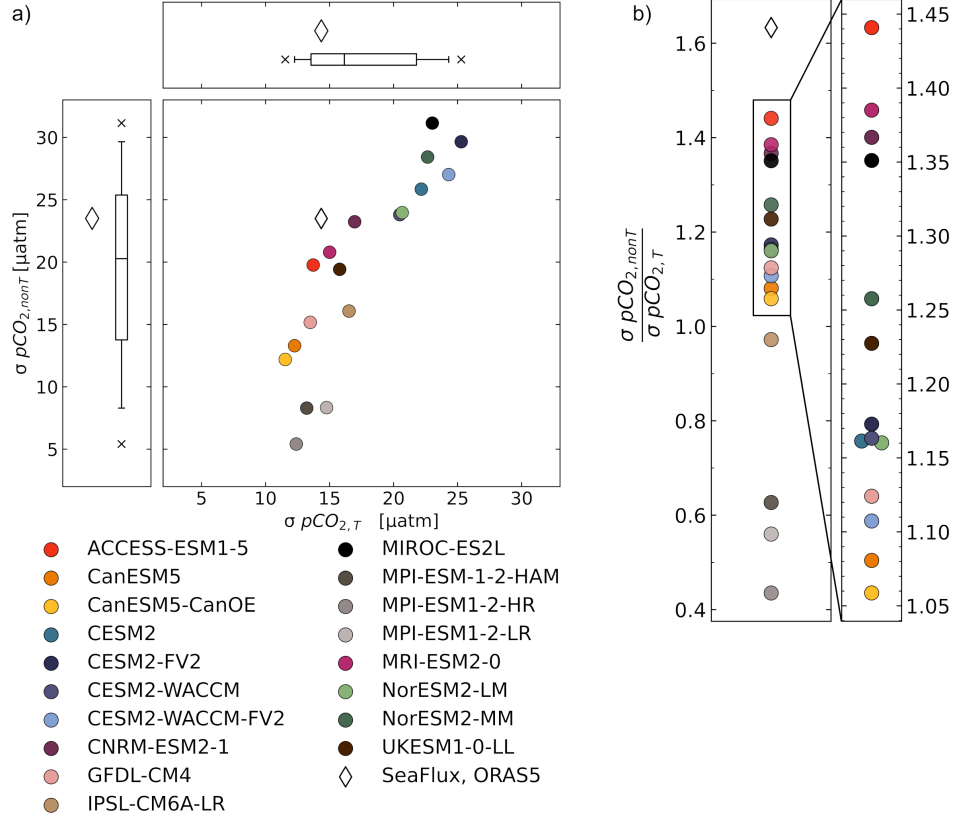


**Figure 7.** a) Amplitudes of pCO<sub>2,T</sub> IAV (x-axis) versus pCO<sub>2,nonT</sub> IAV (y-axis) averaged over the TPI region (units:  $\mu\text{atm}$ ). Model ensemble means are represented by the filled circles, while the unfilled diamond represents the observations-based data products. Box plots around the figure show the distribution among models for pCO<sub>2,T</sub> and pCO<sub>2,nonT</sub> IAV amplitudes. b) Ratios of pCO<sub>2,nonT</sub> to pCO<sub>2,T</sub> IAV amplitudes in models (circles) and in the observations-based data products (diamond). Each scatter point represents the ensemble average for models and SeaFlux. The overlaid rectangle is magnified to see the models better.

in a weak total pCO<sub>2</sub> anomaly in IPSL-CM6A-LR. pCO<sub>2</sub> components in other CMIP6 models are also plotted (Figure S6). A summary plot of the relative amplitudes of the thermal and non-thermal components is shown in Figure 7.

Figure 7a compares the amplitudes of pCO<sub>2,T</sub> and pCO<sub>2,nonT</sub> anomalies across CMIP6 models' ensemble means.  $\sigma pCO_{2,T}$  is 14.4  $\mu\text{atm}$  for SeaFlux-ORAS5, and modeled values range from 11.5 to 25.3  $\mu\text{atm}$ , with the multi-model median variance slightly higher than SeaFlux-ORAS5. On the other hand,  $\sigma pCO_{2,nonT}$  for SeaFlux-ORAS5 is 23.5  $\mu\text{atm}$ , while modeled  $\sigma pCO_{2,nonT}$  ranges from 5.40 to 31.1  $\mu\text{atm}$  with a multi-model median variance lower than that of SeaFlux-ORAS5. Figure 7b compares the ratios of  $\sigma pCO_{2,nonT} : \sigma pCO_{2,T}$  in models against the ratio found in the observations-based data products; SeaFlux-ORAS5 has a ratio of 1.63, while the models all have smaller ratios, ranging from 1.44 (ACCESS-ESM1-5) to 0.44 (MPI-ESM1-2-HR). As such, compared to SeaFlux, modeled  $\sigma pCO_{2,nonT}$  variability are not appropriately balanced against  $\sigma pCO_{2,T}$ . Models with a more dominant non-thermal component, i.e.  $\sigma pCO_{2,nonT} : \sigma pCO_{2,T}$  ratios closer to SeaFlux-ORAS5, have total pCO<sub>2</sub> anomalies that are more negatively correlated with TPI SST anomalies (Figure S6).

### 3.4 pCO<sub>2</sub> Correlations with Other Variables

We evaluate the co-variability of ENSO-related variables with pCO<sub>2</sub> in order to better understand the controls on pCO<sub>2,T</sub> and pCO<sub>2,nonT</sub> in models versus observations-based data products. Reduced upwelling brings less cool, DIC-rich water to the surface, resulting in warmer SSTs and reduced surface ocean pCO<sub>2</sub>. The winds that drive upwelling also force thermocline anomalies; thus,  $z_{\text{therm}}$  anomalies are positive (deeper) in the TPI region when the trades relax and upwelling weakens.

Correlations of SST,  $z_{\text{therm}}$ , and  $w_{50}$  anomalies with pCO<sub>2</sub> anomalies in the TPI region for SeaFlux are consistent with ENSO-driven variability as described above (Figure 8a), indicating that the observations-based products have realistic relationships between these variables and pCO<sub>2</sub>, in particular with SST. For CMIP6, there is a large spread in correlations with pCO<sub>2</sub>. NorESM2-MM and MIROC-ES2L have correlations similar to those seen in the observations-based data products. Models with incorrect correlation signs imply a lack of realistic relationships between these physical variables and pCO<sub>2</sub>. For example, IPSL-CM6A-LR, and the MPI models have incorrect correlation signs between pCO<sub>2</sub> and the variables considered here. Models with the weakest pCO<sub>2,nonT</sub> variances (Figure 7a) tend to be the same models with weak or wrong-sign correlations, or did poorly in other areas throughout this assessment (Figures 3-5). On the other hand, models with the strongest pCO<sub>2,nonT</sub> variances had non-thermal:thermal ratios closest to SeaFlux-ORAS5 (Figure 7). We leave out models that have incorrect correlation signs (negative) for pCO<sub>2</sub> and  $w_{50}$  anomalies (Figure 8) when looking at the vertical transport of DIC, since these models do not have realistic pCO<sub>2</sub>-upwelling relationships.

### 3.5 Vertical Ocean Transport of DIC

Despite having higher pCO<sub>2,nonT</sub> variances in the better performing models, the balances between the non-thermal and thermal components of pCO<sub>2</sub> variability are still not the same as seen in SeaFlux-ORAS5 (Figure 7b). The balance between these components are such that for a given magnitude of pCO<sub>2,T</sub> IAV, the relative magnitude of pCO<sub>2,nonT</sub> IAV in models are insufficient to produce the total pCO<sub>2</sub> IAV seen in SeaFlux. This motivates the rest of this assessment where we take a closer look at the vertical transport of DIC and its contribution to pCO<sub>2,nonT</sub> variability.

In Figure 9a, timeseries for each term in the Reynolds' decomposition (Equation 11) of the vertical transport of DIC in a single model (CESM2) are plotted against the time-tendency of pCO<sub>2,nonT</sub>. Figure 9b shows what can be obtained from data, which is just the second Reynolds term involving the climatological vertical DIC gradient and variable upwelling (Equation 11, second term on right). With Reynolds' decomposition, we are able to isolate in models the contributions from variability in the vertical DIC gradient (Figure 9a: first panel) and the contributions from upwelling variability (Figure 9a: second panel) to the time-tendency of pCO<sub>2,nonT</sub>,  $\partial_t \text{pCO}_{2,\text{nonT}}'$ . The non-linear term (Figure 9a: third panel) is small. The fourth panel in Figure 9a compares the total anomaly of the vertical ocean transport of DIC against  $\partial_t \text{pCO}_{2,\text{nonT}}'$ . In CESM2, the first two Reynolds terms are roughly the same in magnitude, with standard deviations 2.65 and 2.77 times larger than the standard deviation of  $\partial_t \text{pCO}_{2,\text{nonT}}'$ . The non-linear term is approximately the same magnitude as  $\partial_t \text{pCO}_{2,\text{nonT}}'$ . The total anomaly (Figure 9a: fourth panel) has a standard deviation five times larger than the standard deviation of  $\partial_t \text{pCO}_{2,\text{nonT}}'$ , and has a positive correlation of  $r = 0.70$ . The magnitude of the total anomaly in vertical DIC transport means that it is important to pCO<sub>2,nonT</sub> variability, and also that there must be strong damping terms. A summary of the Reynolds' terms in other models is in Table S2. Other models have similar results as CESM2 in that the total anomaly of vertical transport of DIC is significant in magnitude relative to the magnitude of pCO<sub>2,nonT</sub> variability. Values of their relative magnitudes,  $\sigma_{\text{ratio}}$ , range from 2.94 to 5.55 (Table S2),

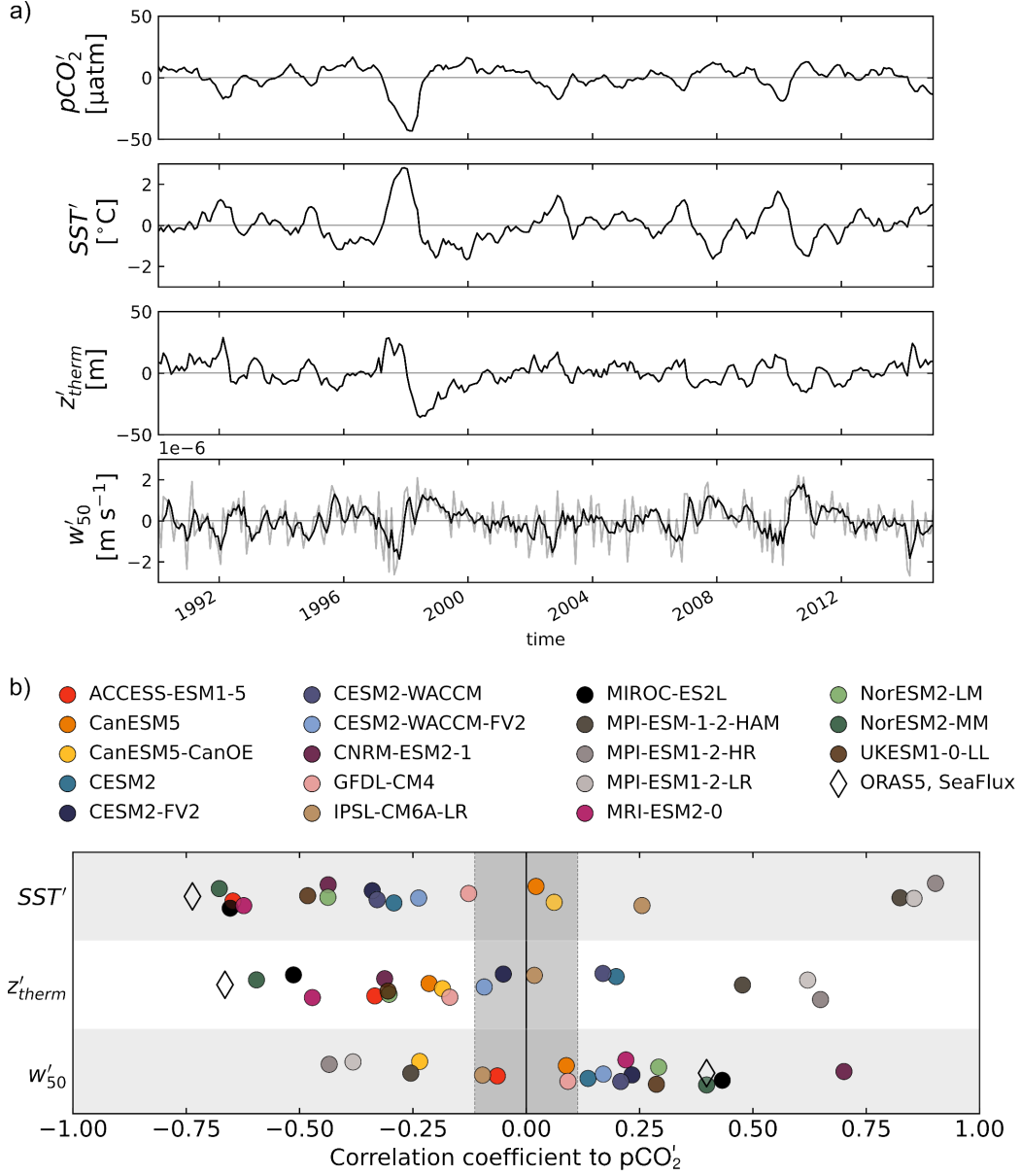


**Figure 8.** a) Observed timeseries of  $p\text{CO}_2$  (units:  $\mu\text{atm}$ ), SST (units:  $^{\circ}\text{C}$ ),  $z_{\text{therm}}$  (units: m), and  $w_{50}$  anomalies (units:  $\text{ms}^{-1}$ ) from SeaFlux and ORAS5. A 3-month running mean of  $w_{50}$  anomalies is also shown (fourth panel). b) Correlations of  $p\text{CO}_2$  to SST,  $z_{\text{therm}}$ , and  $w_{50}$  monthly anomalies over the TPI region. Correlation coefficients for the observations-based data products are marked by the clear diamonds, and the 18 CMIP6 models are marked by filled circles. The model correlation coefficients shown are ensemble means. The grey shading indicates the 95% confidence threshold for the correlations.

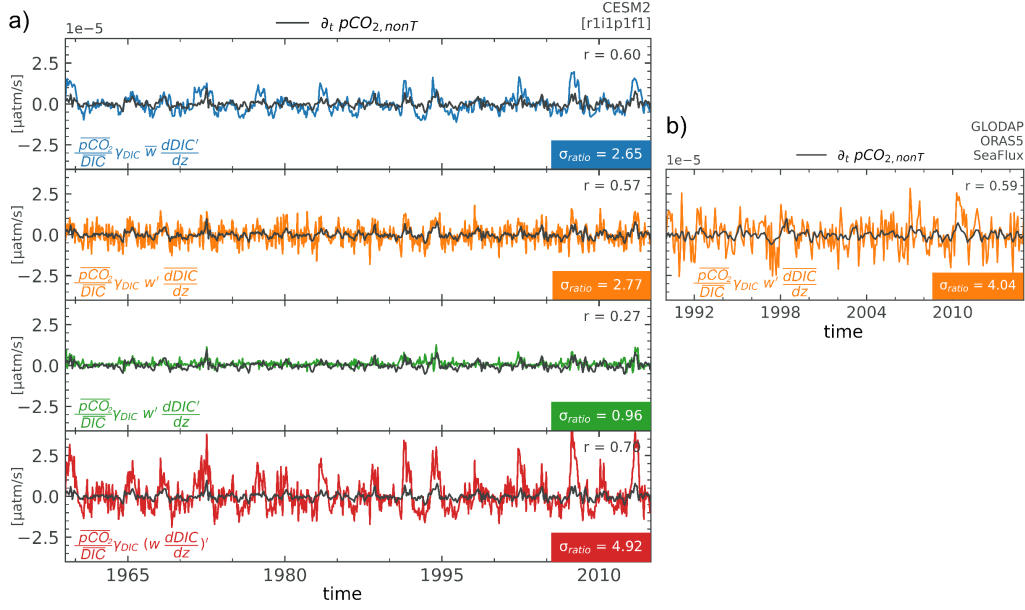


**Figure 9.** a) Timeseries of the first (blue), second (orange) and third (green) Reynolds' terms from Equation 11, and the full variability is shown in the bottom panel (red) for one member from CESM2 (units:  $\mu\text{atm s}^{-1}$ ). The time-tendency of  $p\text{CO}_{2,nonT}$  is shown in every panel (black line).  $\sigma_{\text{ratio}} = \sigma(\text{Reynolds' term}) / \sigma \partial_t p\text{CO}_{2,nonT}$  is annotated in every panel. The correlation coefficient (r) between the timeseries are also shown. For the other models, a summary of this information can be found in Table S2. b) timeseries of the second Reynolds' term computed from observations-based data products.

which together with strong correlations, means that variability in the vertical transport of DIC is an important source of  $p\text{CO}_{2,nonT}$  variability.

Across the models, the first two Reynolds' terms,  $\overline{w}_{50} \partial_z \text{DIC}'$  and  $w'_{50} \overline{\partial_z \text{DIC}}$ , are the largest terms (Table S2), which suggests that the variability in both upwelling and vertical DIC gradients are similarly important to  $p\text{CO}_{2,nonT}$  variability. In MIROC-ES2L, the non-linear term is almost the same amplitude as the first two terms. For observations-based data products, the second Reynolds term ( $w'_{50} \overline{\partial_z \text{DIC}}$ ) has a standard deviation four times bigger than the standard deviation of the observations-based  $\partial_t p\text{CO}_{2,nonT}$  (Figure 9b). Compared to the observations-based data products, the  $w'_{50} \overline{\partial_z \text{DIC}}$  term is weak in models (Table S2, second column), except for UKESM1-0-LL. This could be due to either a weak vertical gradient of climatological DIC, or weak upwelling variability, or a combination of both.

A time-averaged vertical velocity section from ORAS5 (Figure S7a) reveals that the depth at which upwelling occurs is within the upper 100m, with a maxima between 50 to 75m at 220°E. We compare upwelling variability in models versus ORAS5 in Figure 10a at 50m. We find that the range of upwelling variability across models is comparable and inclusive of the upwelling variability seen in ORAS5. In contrast, Figure 10b compares the vertical gradient of climatological DIC at 50 m to GLODAPv2. All the models have weaker gradients. We repeat this comparison at 80 m (Figure S8) and confirm that it is robust. Modeled vertical gradients of climatological DIC are biased weak, causing the second Reynolds term ( $w'_{50} \overline{\partial_z \text{DIC}}$ ) in models to be weaker than the observations-based estimate (Figure 9; Table S2). To summarize, the second Reynold's term ( $w'_{50} \overline{\partial_z \text{DIC}}$ ) is an important term in the overall variability of the vertical transport of DIC, which is



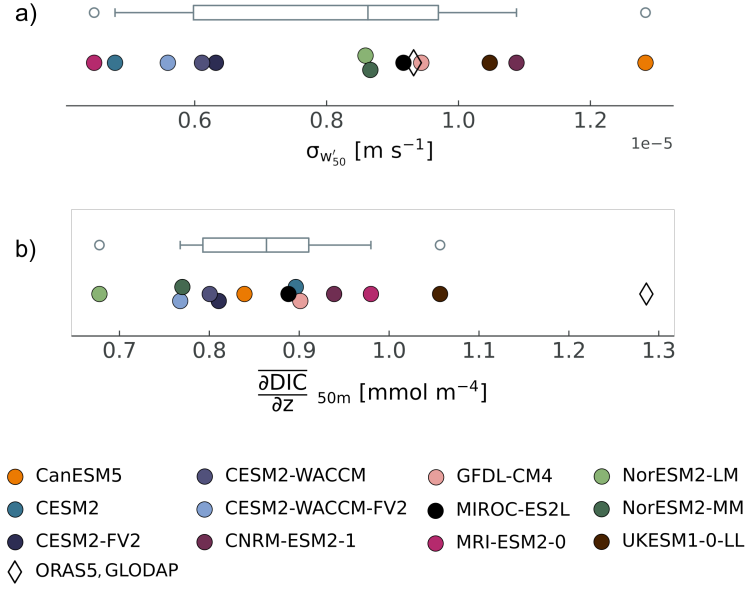


**Figure 10.** a) Amplitudes (units:  $\text{ms}^{-1}$ ) of upwelling IAV across models (filled circles are one member per model) versus ORAS5 (diamond). b) Amplitudes (units:  $\text{mmolm}^{-4}$ ) of vertical gradients of climatological DIC across models versus GLODAPv2. The boxplots represent the CMIP6 models.

important to the variability in  $\text{pCO}_{2,\text{non}T}$ , and thus  $\text{pCO}_2$  variability. Underestimations in  $w'_{50}\partial_z\overline{\text{DIC}}$  may result in an underestimation in  $\text{pCO}_2$  variability.

Alongside modeled mean vertical DIC gradients, we plot the mean vertical temperature gradients ( $\partial_z\overline{T}$ ) at 50m depth to compare the relative strengths of gradients in models, and to identify model biases from observations-based data products (Figure 11a). Vertical temperature gradients are negative since ocean temperatures decrease with depth. The spread in strengths of modeled temperature gradients encompasses that seen in ORAS5, though the majority of models have weaker temperature gradients. The percentage difference between ORAS5 and the models' median temperature gradient is about 21%. For the vertical gradient of climatological DIC, all models underestimate it compared to GLODAPv2, and the ensemble median has a percentage difference of about 39%. While the models tend to underestimate both the vertical gradients of climatological DIC and temperature, the climatological DIC gradients are more weakly biased, which for a given upwelling will tend to result in weaker  $\text{pCO}_{2,\text{non}T}$  variability relative to  $\text{pCO}_{2,T}$ .

Figure 11b compares the influence of  $w'_{50}\partial_z\overline{T}$  against the influence of  $w'_{50}\partial_z\overline{\text{DIC}}$  on  $\text{pCO}_2$  using the coefficients from Equation 7. Contributions from  $w'_{50}\partial_z\overline{\text{DIC}}$  to  $\text{pCO}_2$  in models are about 6 times greater than the thermal contributions. The vertical DIC term is much bigger than the vertical T term, but the associated  $\text{pCO}_{2,\text{non}T}$  variability is not proportionally bigger than  $\text{pCO}_{2,T}$  variability. Thus, weak vertical gradients cannot fully explain the  $\text{pCO}_{2,\text{non}T}$ ,  $\text{pCO}_{2,T}$  differences. Daily  $\text{pCO}_2$  variability ( $\sigma p\text{CO}_2$ ) in the TPI region in SeaFlux is  $0.35 \mu\text{atm day}^{-1}$ , and values in models range from 0.29 to  $0.46 \mu\text{atm day}^{-1}$  (not shown). These values of daily TPI  $\text{pCO}_2$  variability are on the same order of magnitude as the  $w'_{50}\partial_z\overline{\text{DIC}}$  contributions to  $\text{pCO}_2$  (Figure 11b: y-axis). In observations, and in some models,  $w'_{50}\partial_z\overline{\text{DIC}}$  contributions to  $\text{pCO}_2$  are greater than the daily  $\text{pCO}_2$  variability in the TPI region. In observations, and in some models,  $w'_{50}\partial_z\overline{\text{DIC}}$  contributions to  $\text{pCO}_2$  are larger than daily  $\text{pCO}_2$  variability in the TPI region. This

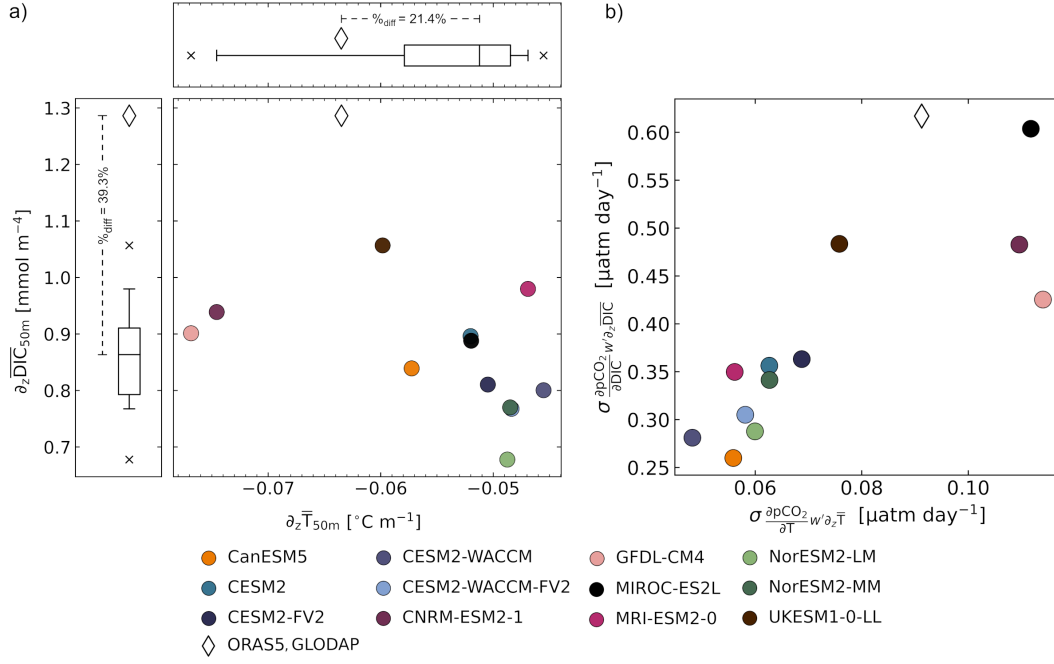


**Figure 11.** a) The relative strength of vertical mean temperature gradients (x-axis, units:  $^{\circ}\text{C m}^{-1}$ ) against vertical climatological DIC gradients (y-axis, units:  $\text{mmol m}^{-4}$ ) in 12 CMIP6 models (filled circles represent a single ensemble member) and in ORAS5 versus GLODAPv2 data (clear diamond). The boxplots represent the distribution in gradients among models, excluding observations-based data products (clear diamonds). b) The vertical transport of the climatological vertical temperature gradient versus the DIC gradient, converted into units of  $\mu\text{atm day}^{-1}$ .

means that significant damping of  $\text{pCO}_2$  must be happening in order for it to be underestimated, despite the large contribution from the vertical transport of DIC.

## 4 Discussion

The majority (15) of the 18 CMIP6 models underestimate  $\text{pCO}_2$  IAV, while they overestimate SST IAV.  $\text{FCO}_2$  IAV is also underestimated by the majority of CMIP6 models. Previous studies of historical simulations from the earlier CMIP5 found that  $\text{FCO}_2$  IAV were also underestimated in models (Dong et al., 2016, 2017). Results from another CMIP6 study also find that most models simulate weak  $\text{FCO}_2$  anomalies while overestimating SST IAV (Vaithinada Ayar et al., 2022).

We find that the correlations between  $\text{pCO}_2$  and other ENSO-related variables vary. Most models have correlations weaker than observed over the TPI region, a few are consistent with observations, and another few are opposite to observed. Weak ENSO-driven relationships were also noted in previous CMIP5 studies (Dong et al., 2017; Jin et al., 2019). Dong et al. (2016) also found that 12 models out of the 18 CMIP5 subset failed to show ENSO characteristics in  $\text{FCO}_2$  variability. They also found that models differed among themselves the most in regions with strong vertical movement, such as the tropical Pacific.

Modeled  $\text{pCO}_{2,\text{non}T}$  variance in CMIP6 is not appropriately balanced with  $\text{pCO}_{2,T}$  variability. Weak  $\text{pCO}_{2,\text{non}T}$  anomalies are insufficient to counteract the  $\text{pCO}_{2,T}$  anomaly



lies resulting in total  $p\text{CO}_2$  anomalies that are too weak. In the equatorial Pacific, Jin et al. (2019) found  $p\text{CO}_2$  biases in two CMIP5 models that resulted from weak DIC contributions to  $p\text{CO}_2$ . Weak DIC contributions were found to be mainly caused by weak vertical gradients of climatological DIC and weak upwelling anomalies, which both limit the vertical transport of DIC (Jin et al., 2019). We find that upwelling anomalies in CMIP6 are comparable to ORAS5 (Figure 10a).

Changes in the vertical transport of DIC affects surface DIC variability, which is known to be the dominant driver of  $p\text{CO}_2$  variability in the surface equatorial Pacific Ocean (McKinley et al., 2004; Liao et al., 2020). We find model  $p\text{CO}_2$  anomalies due to variability in the vertical transport of DIC are larger than their  $p\text{CO}_{2,nonT}$  anomalies by a factor of 3 to almost 6 times (see Table S2: last column) but are positively correlated. This suggests that variability in the vertical transport of DIC is an important source of  $p\text{CO}_{2,nonT}$  variability in models. At the same time,  $w'_{50}\partial_z\overline{\text{DIC}}$  contributions to  $p\text{CO}_2$  are comparable in magnitude to daily  $p\text{CO}_2$  variability in the TPI region (Figure S9b). Together, these findings indicate that  $w'_{50}\partial_z\overline{\text{DIC}}$  contributions to  $p\text{CO}_2$  variability are significantly damped by other processes.

The vertical gradient of climatological DIC is consistently weak across all the models relative to observations-based data products (Figure 10), which is consistent with prior model results from CMIP5 (Jin et al., 2019). Vertical gradients of climatological temperature are not as weak. The imbalance in the relative strengths of these vertical gradients, for a given upwelling anomaly, contributes towards weaker non-thermal  $p\text{CO}_2$  variability, relative to the thermal.

While the relative strengths of mean vertical gradients, through upwelling, can result in weaker  $\sigma p\text{CO}_{2,nonT}:\sigma p\text{CO}_{2,T}$  ratios, we do not find a linear scaling between the relative strengths in mean vertical gradients and the ratios of  $\sigma p\text{CO}_{2,nonT}:\sigma p\text{CO}_{2,T}$  across the models (Figure S9). A linear scaling would indicate that biases in the relative strengths of the mean vertical gradients proportionally bias the  $p\text{CO}_2$  ratios. Thus, we find the relative strengths of mean vertical gradients alone do not determine the imbalance in  $p\text{CO}_2$  ratios. A more complete assessment that includes the other processes that contribute to  $p\text{CO}_2$  variability will be necessary to understand the causes of insufficient  $p\text{CO}_{2,nonT}$  variability.

Other processes that contribute to equatorial Pacific DIC variability that can dampen  $p\text{CO}_{2,nonT}$  variability, include the horizontal transport of DIC, biological processes, freshwater fluxes and air-sea  $\text{CO}_2$  fluxes. For example, when DIC is brought to the surface via upwelling, though  $p\text{CO}_2$  increases, the instantaneous air-sea  $\text{CO}_2$  flux response dampens surface DIC concentrations (Liao et al., 2020). The biological response also damps surface DIC concentrations; upwelling of nutrient-rich waters enhances biologically-driven uptake of DIC (Chavez et al., 1999). Freshwater fluxes (rainfall) also dilute surface DIC concentrations, and westward horizontal transport along the equator removes DIC from the upwelling region (Doney et al., 2009).

Aside from DIC, other ocean biogeochemical variables influence surface  $p\text{CO}_{2,nonT}$ , such as alkalinity. Vaittinada Ayar et al. (2022) find that models with strong alkalinity biases have weak surface DIC biases (i.e. weak surface DIC variability), which leads to a reduction in  $p\text{CO}_{2,nonT}$  variability. They find that for some models (CanESM5, GFDL-CM4 and MRI-ESM2-0),  $p\text{CO}_{2,nonT}$  variability is weak enough that  $p\text{CO}_T$  variability can dominate total  $p\text{CO}_2$  anomalies. However, an alkalinity bias alone does not explain all the models that underestimate  $p\text{CO}_{2,nonT}$ , relative to  $p\text{CO}_{2,T}$ , as we analyze here. For example, Vaittinada Ayar et al. (2022) shows that IPSL-CM6A-LR doesn't have a strong alkalinity bias, however, we find that its  $p\text{CO}_{2,nonT}:p\text{CO}_{2,T}$  variance ratio is weaker than the ratio in MRI-ESM2-0 (Figure 7b), which is a model they show with a strong alkalinity bias.

Vaithinada Ayar et al. (2022) proposed that models without a strong alkalinity bias may be better predictors of future ENSO-CO<sub>2</sub> flux dynamics. However, we find that these models underestimate equatorial Pacific pCO<sub>2</sub> IAV and ENSO-related covariability. For example, IPSL-CM6A-LR did not have realistic correlations between pCO<sub>2</sub> and SST,  $z_{\text{therm}}$  or  $w_{50}$  anomalies (Figure 8b). We propose that a wide range of variables need to be considered when selecting models for analysis of future trends. While this study looks at ENSO-driven pCO<sub>2</sub> IAV, it has relevance for trends. Trends in SSTs, thermocline depths and upwelling in response to rising atmospheric CO<sub>2</sub> involve many of the same coupled dynamics that drive ENSO variability (Seager et al., 2019; Cane et al., 1997; Clement et al., 1996). CMIP6 models cannot reproduce the observed trends in the tropical Pacific physical state and hence it is possible that they are also misrepresenting the trends in pCO<sub>2</sub> and air-sea CO<sub>2</sub> fluxes, with potential influence on the airborne fraction of anthropogenic CO<sub>2</sub>. Validating ENSO-driven pCO<sub>2</sub> variability in models is a necessary first step to examining the tropical Pacific’s coupled climate-carbon response to anthropogenic climate change.

## 5 Conclusions

In the equatorial Pacific, weak ENSO-related pCO<sub>2</sub> variability in CMIP6 models is explained by an imbalance between pCO<sub>2,*nonT*</sub> and pCO<sub>2,*T*</sub> anomalies, whereby pCO<sub>2,*nonT*</sub> variability is insufficient to counteract strong pCO<sub>2,*T*</sub> variability. Strong pCO<sub>2,*T*</sub> variability in CMIP6 is driven by excessive SST variance. Variability in the vertical transport of DIC does matter to pCO<sub>2,*nonT*</sub> variability in that upwelling anomalies acting on weak vertical DIC gradients can lead to weaker surface DIC variability. However, this alone does not explain the relative magnitudes of pCO<sub>2,*nonT*</sub> and pCO<sub>2,*T*</sub> anomalies. To guide model development, assessments of other processes that drive DIC variability will help to identify the causes of significant damping of pCO<sub>2,*nonT*</sub> variability that ultimately leads to weak pCO<sub>2</sub> variability in models.

## 6 Open Research

CMIP6 model output data are available at: <http://esgf-node.llnl.gov/projects/cmip6>. Information on installing and using the CMIP6 data pre-processing Python package (Busecke & Abernathey, 2020) can be accessed here: <https://cmip6-preprocessing.readthedocs.io/en/latest/>.

SeaFlux products (including wind speed products) are available on Zenodo: <https://doi.org/10.5281/zenodo.5482547>. GLODAPv2.2021 data, archived at NOAA-NCEI at <https://www.ncei.noaa.gov/access/metadata/landing-page/bin/iso?id=gov.noaa.nodc:0237935>, can also be downloaded from the GLODAP website: <https://www.glodap.info/>. The ECMWF-ORAS5 data set can be downloaded from the Integrated Climate Data Center portal at <http://icdc.cen.uni-hamburg.de/thredds/catalog/ftpthredds/EASYInit/oras5/catalog.html> and <https://www.cen.uni-hamburg.de/icdc/data/ocean/easy-init-ocean/ecmwf-oras5-backward-extension.html> for 1979-2018 and 1958-1978, respectively. HadISST data were obtained from <https://www.metoffice.gov.uk/hadobs/hadisst/> and are © British Crown Copyright, Met Office (2022), provided under a Non-Commercial Government Licence <http://www.nationalarchives.gov.uk/doc/non-commercial-government-licence/version/2/>.

## Acknowledgments

We acknowledge the World Climate Research Programme, which, through its Working Group on Coupled Modelling, coordinated and promoted CMIP6. We thank the climate modeling groups for producing and making available their model output, the Earth System Grid Federation (ESGF) for archiving the data and providing access, and the multiple funding agencies who support CMIP6 and ESGF. S.W. acknowledges Pangeo for providing cloud-services for this research, and would also like to thank Julius Busecke for their CMIP6 pre-processing Python package. This research was supported in part by the National Science Foundation (OCE 22-19829, OCE-1948624, LEAP STC 2019625). The authors declare that they have no conflict of interest.

## References

- Bentsen, M., Olivière, D. J. L., Seland, y., Toniazzo, T., Gjermundsen, A., Graff, L. S., ... Schulz, M. (2019). *NCC NorESM2-MM model output prepared for CMIP6 CMIP historical [Dataset]*. Earth System Grid Federation. doi: 10.22033/ESGF/CMIP6.8040
- Bjerknes, J. (1966). A possible response of the atmospheric hadley circulation to equatorial anomalies of ocean temperature. *Tellus*, 18(4), 820-829. Retrieved from <https://onlinelibrary.wiley.com/doi/abs/10.1111/j.2153-3490.1966.tb00303.x> doi: <https://doi.org/10.1111/j.2153-3490.1966.tb00303.x>
- Boucher, O., Denvil, S., Levavasseur, G., Cozic, A., Caubel, A., Foujols, M.-A., ... Marchand, M. (2021). *IPSL IPSL-CM6A-LR-INCA model output prepared for CMIP6 CMIP historical [Dataset]*. Earth System Grid Federation. doi: 10.22033/ESGF/CMIP6.13601
- Busecke, J., & Abernathey, R. (2020). Cmpip6 without the interpolation: Grid-native analysis with pangeo in the cloud. *Earth and Space Science Open Archive*, 1. Retrieved from <https://doi.org/10.1002/essoar.10504242.1> doi: 10.1002/essoar.10504242.1
- Byun, Y.-H. (2020). *NIMS-KMA UKESM1.0-LL model output prepared for CMIP6 CMIP historical [Dataset]*. Earth System Grid Federation. doi: 10.22033/ESGF/CMIP6.8379
- Cane, M. A., Clement, A. C., Kaplan, A., Kushnir, Y., Pozdnyakov, D., Seager, R., ... Murtugudde, R. (1997). Twentieth-century sea surface temperature trends. *Science*, 275(5302), 957-960. Retrieved from <https://www.science.org/doi/>

- abs/10.1126/science.275.5302.957 doi: 10.1126/science.275.5302.957
- Chavez, F. P., Strutton, P. G., Friederich, G. E., Feely, R. A., Feldman, G. C., Foley, D. G., & McPhaden, M. J. (1999). Biological and chemical response of the equatorial pacific ocean to the 1997-98 el niño. *Science*, 286(5447), 2126-2131. Retrieved from <https://www.science.org/doi/abs/10.1126/science.286.5447.2126> doi: 10.1126/science.286.5447.2126
- Clement, A. C., Seager, R., Cane, M. A., & Zebiak, S. E. (1996). An ocean dynamical thermostat. *Journal of Climate*, 9(9), 2190 - 2196. Retrieved from [https://journals.ametsoc.org/view/journals/clim/9/9/1520-0442\\_1996\\_009\\_2190\\_aodt\\_2\\_0\\_co\\_2.xml](https://journals.ametsoc.org/view/journals/clim/9/9/1520-0442_1996_009_2190_aodt_2_0_co_2.xml) doi: 10.1175/1520-0442(1996)009<2190:AODT>2.0.CO;2
- Danabasoglu, G. (2019a). *NCAR CESM2-FV2 model output prepared for CMIP6 CMIP historical [Dataset]*. Earth System Grid Federation. doi: 10.22033/ESGF/CMIP6.11297
- Danabasoglu, G. (2019b). *NCAR CESM2 model output prepared for CMIP6 CMIP historical [Dataset]*. Earth System Grid Federation. doi: 10.22033/ESGF/CMIP6.7627
- Danabasoglu, G. (2019c). *NCAR CESM2-WACCM-FV2 model output prepared for CMIP6 CMIP historical [Dataset]*. Earth System Grid Federation. doi: 10.22033/ESGF/CMIP6.11298
- Danabasoglu, G. (2019d). *NCAR CESM2-WACCM model output prepared for CMIP6 CMIP historical [Dataset]*. Earth System Grid Federation. doi: 10.22033/ESGF/CMIP6.10071
- Doney, S. C., Lima, I., Feely, R. A., Glover, D. M., Lindsay, K., Mahowald, N., ... Wanninkhof, R. (2009). Mechanisms governing interannual variability in upper-ocean inorganic carbon system and air-sea co<sub>2</sub> fluxes: Physical climate and atmospheric dust. *Deep Sea Research Part II: Topical Studies in Oceanography*, 56(8), 640-655. (Surface Ocean CO<sub>2</sub> Variability and Vulnerabilities) doi: <https://doi.org/10.1016/j.dsr2.2008.12.006>
- Dong, F., Li, Y., & Wang, B. (2017). Assessment of responses of tropical pacific air-sea co<sub>2</sub> flux to enso in 14 cmip5 models. *Journal of Climate*, 30(21), 8595 - 8613. Retrieved from <https://journals.ametsoc.org/view/journals/clim/30/21/jcli-d-16-0543.1.xml> doi: 10.1175/JCLI-D-16-0543.1
- Dong, F., Li, Y., Wang, B., Huang, W., Shi, Y., & Dong, W. (2016). Global air-sea co<sub>2</sub> flux in 22 cmip5 models: Multiyear mean and interannual variability. *Journal of Climate*, 29(7), 2407-2431.
- Emori, S., Taylor, K., Hewitson, B., Zermoglio, F., Jukes, M., Lautenschlager, M., & Stockhause, M. (2016). Cmp5 data provided at the ipcc data distribution centre [Computer software manual]. Fact Sheet of the Task Group on Data and Scenario Support for Impact and Climate Analysis (TGICA) of the Intergovernmental Panel on Climate Change (IPCC). Retrieved from [http://sedac.ipcc-data.org/ddc/ar5\\_scenario\\_process/RCPs.html](http://sedac.ipcc-data.org/ddc/ar5_scenario_process/RCPs.html)
- Farneti, R., Stiz, A., & Ssebandeke, J. B. (2022, 12). Improvements and persistent biases in the southeast tropical atlantic in cmip models. *npj Climate and Atmospheric Science*, 5. doi: 10.1038/s41612-022-00264-4
- Fay, A. R., Gregor, L., Landschützer, P., McKinley, G. A., Gruber, N., Gehlen, M., ... Zeng, J. (2021). Seaflux: harmonization of air-sea co<sub>2</sub> fluxes from surface pco<sub>2</sub> data products using a standardized approach. *Earth System Science Data*, 13(10), 4693-4710. Retrieved from <https://essd.copernicus.org/articles/13/4693/2021/> doi: 10.5194/essd-13-4693-2021
- Feely, R. A., Takahashi, T., Wanninkhof, R., McPhaden, M. J., Cosca, C. E., Sutherland, S. C., & Carr, M.-E. (2006). Decadal variability of the air-sea co<sub>2</sub> fluxes in the equatorial pacific ocean. *Journal of Geophysical Research: Oceans*, 111(C8). Retrieved from <https://agupubs.onlinelibrary.wiley.com/doi/abs/10.1029/2005JC003129> doi: <https://doi.org/10.1029/2005JC003129>

- 2005JC003129
- Friedlingstein, P., Jones, M. W., O'Sullivan, M., Andrew, R. M., Bakker, D. C. E., Hauck, J., ... Zeng, J. (2022). Global carbon budget 2021. *Earth System Science Data*, 14(4), 1917–2005. Retrieved from <https://essd.copernicus.org/articles/14/1917/2022/> doi: 10.5194/essd-14-1917-2022
- Guo, H., John, J. G., Blanton, C., McHugh, C., Nikonov, S., Radhakrishnan, A., ... Zhang, R. (2018). *NOAA-GFDL GFDL-CM4 model output historical [Dataset]*. Earth System Grid Federation. doi: 10.22033/ESGF/CMIP6.8594
- Hajima, T., Abe, M., Arakawa, O., Suzuki, T., Komuro, Y., Ogura, T., ... Tachiiri, K. (2019). *MIROC MIROC-ES2L model output prepared for CMIP6 CMIP historical [Dataset]*. Earth System Grid Federation. doi: 10.22033/ESGF/CMIP6.5602
- Jin, C., Zhou, T., & Chen, X. (2019). Can cmip5 earth system models reproduce the interannual variability of air-sea co<sub>2</sub> fluxes over the tropical pacific ocean? *Journal of Climate*, 32(8), 2261 - 2275. Retrieved from <https://journals.ametsoc.org/view/journals/clim/32/8/jcli-d-18-0131.1.xml> doi: 10.1175/JCLI-D-18-0131.1
- Jungclaus, J., Bittner, M., Wieners, K.-H., Wachsmann, F., Schupfner, M., Legutke, S., ... Roeckner, E. (2019). *MPI-M MPI-ESM1.2-HR model output prepared for CMIP6 CMIP historical [Dataset]*. Earth System Grid Federation. doi: 10.22033/ESGF/CMIP6.6594
- Landschützer, P., Gruber, N., & Bakker, D. C. E. (2016). Decadal variations and trends of the global ocean carbon sink. *Global Biogeochemical Cycles*, 30(10), 1396-1417. Retrieved from <https://agupubs.onlinelibrary.wiley.com/doi/abs/10.1002/2015GB005359> doi: <https://doi.org/10.1002/2015GB005359>
- Lauvset, S. K., Lange, N., Tanhua, T., Bittig, H. C., Olsen, A., Kozyr, A., ... Key, R. M. (2021). An updated version of the global interior ocean biogeochemical data product, glodapv2.2021. *Earth System Science Data*, 13(12), 5565–5589. Retrieved from <https://essd.copernicus.org/articles/13/5565/2021/> doi: 10.5194/essd-13-5565-2021
- Le Quéré, C., Orr, J. C., Monfray, P., Aumont, O., & Madec, G. (2000). Interannual variability of the oceanic sink of co<sub>2</sub> from 1979 through 1997. *Global Biogeochemical Cycles*, 14(4), 1247–1265.
- Li, G., & Xie, S.-P. (2012). Origins of tropical-wide sst biases in cmip multi-model ensembles. *Geophysical Research Letters*, 39(22). Retrieved from <https://agupubs.onlinelibrary.wiley.com/doi/abs/10.1029/2012GL053777> doi: <https://doi.org/10.1029/2012GL053777>
- Liao, E., Resplandy, L., Liu, J., & Bowman, K. W. (2020). Amplification of the ocean carbon sink during el niños: Role of poleward ekman transport and influence on atmospheric co<sub>2</sub>. *Global Biogeochemical Cycles*, 34(9), e2020GB006574. Retrieved from <https://agupubs.onlinelibrary.wiley.com/doi/abs/10.1029/2020GB006574> doi: <https://doi.org/10.1029/2020GB006574>
- Long, M. C., Lindsay, K., Peacock, S., Moore, J. K., & Doney, S. C. (2013). Twentieth-century oceanic carbon uptake and storage in cesm1(bgc). *Journal of Climate*, 26(18), 6775 - 6800. Retrieved from <https://journals.ametsoc.org/view/journals/clim/26/18/jcli-d-12-00184.1.xml> doi: 10.1175/JCLI-D-12-00184.1
- Lovenduski, N. S., Gruber, N., Doney, S. C., & Lima, I. D. (2007). Enhanced co<sub>2</sub> outgassing in the southern ocean from a positive phase of the southern annular mode. *Global Biogeochemical Cycles*, 21(2). Retrieved from <https://agupubs.onlinelibrary.wiley.com/doi/abs/10.1029/2006GB002900> doi: <https://doi.org/10.1029/2006GB002900>
- McKinley, G. A., Fay, A. R., Lovenduski, N. S., & Pilcher, D. J. (2017). Natural



- variability and anthropogenic trends in the ocean carbon sink. *Annual Review of Marine Science*, 9(1), 125-150. Retrieved from <https://doi.org/10.1146/annurev-marine-010816-060529> (PMID: 27620831) doi: 10.1146/annurev-marine-010816-060529
- McKinley, G. A., Follows, M. J., & Marshall, J. (2004, June). Mechanisms of air-sea CO<sub>2</sub> flux variability in the equatorial Pacific and the North Atlantic. *Global Biogeochemical Cycles*, 18(2), GB2011. doi: 10.1029/2003GB002179
- Neubauer, D., Ferrachat, S., Siegenthaler-Le Drian, C., Stoll, J., Folini, D. S., Tegen, I., ... Lohmann, U. (2019). *HAMMOZ-Consortium MPI-ESM1.2-HAM model output prepared for CMIP6 CMIP historical [Dataset]*. Earth System Grid Federation. doi: 10.22033/ESGF/CMIP6.5016
- Rayner, N. A., Parker, D. E., Horton, E. B., Folland, C. K., Alexander, L. V., Rowell, D. P., ... Kaplan, A. (2003). Global analyses of sea surface temperature, sea ice, and night marine air temperature since the late nineteenth century. *Journal of Geophysical Research: Atmospheres*, 108(D14). Retrieved from <https://agupubs.onlinelibrary.wiley.com/doi/abs/10.1029/2002JD002670> doi: <https://doi.org/10.1029/2002JD002670>
- Resplandy, L., Séférian, R., & Bopp, L. (2015). Natural variability of co<sub>2</sub> and o<sub>2</sub> fluxes: What can we learn from centuries-long climate models simulations? *Journal of Geophysical Research: Oceans*, 120(1), 384-404. Retrieved from <https://agupubs.onlinelibrary.wiley.com/doi/abs/10.1002/2014JC010463> doi: <https://doi.org/10.1002/2014JC010463>
- Rödenbeck, C., Bakker, D. C. E., Metzl, N., Olsen, A., Sabine, C., Cassar, N., ... Heimann, M. (2014). Interannual sea-air co<sub>2</sub> flux variability from an observation-driven ocean mixed-layer scheme. *Biogeosciences*, 11(17), 4599-4613. Retrieved from <https://bg.copernicus.org/articles/11/4599/2014/> doi: 10.5194/bg-11-4599-2014
- Sarmiento, J. L., & Gruber, N. (2006). *Ocean biogeochemical dynamics*. Princeton University Press.
- Seager, R., Cane, M., Henderson, N., Lee, D. E., Abernathey, R., & Zhang, H. (2019, 7). Strengthening tropical pacific zonal sea surface temperature gradient consistent with rising greenhouse gases. *Nature Climate Change*, 9, 517-522. doi: 10.1038/s41558-019-0505-x
- Seferian, R. (2018). *CNRM-CERFACS CNRM-ESM2-1 model output prepared for CMIP6 CMIP historical [Dataset]*. Earth System Grid Federation. doi: 10.22033/ESGF/CMIP6.4068
- Séférian, R., Berthet, S., Yool, A., Palmieri, J., Bopp, L., Tagliabue, A., ... others (2020). Tracking improvement in simulated marine biogeochemistry between cmip5 and cmip6. *Current Climate Change Reports*, 6(3), 95-119.
- Seland, y., Bentsen, M., Olivie, D. J. L., Toniazzo, T., Gjermundsen, A., Graff, L. S., ... Schulz, M. (2019). *NCC NorESM2-LM model output prepared for CMIP6 CMIP historical [Dataset]*. Earth System Grid Federation. Retrieved from <https://doi.org/10.22033/ESGF/CMIP6.8036> doi: 10.22033/ESGF/CMIP6.8036
- Sutton, A. J., Feely, R. A., Sabine, C. L., McPhaden, M. J., Takahashi, T., Chavez, F. P., ... Mathis, J. T. (2014). Natural variability and anthropogenic change in equatorial pacific surface ocean pco<sub>2</sub> and ph. *Global Biogeochemical Cycles*, 28(2), 131-145. Retrieved from <https://agupubs.onlinelibrary.wiley.com/doi/abs/10.1002/2013GB004679> doi: <https://doi.org/10.1002/2013GB004679>
- Swart, N. C., Cole, J. N., Kharin, V. V., Lazare, M., Scinocca, J. F., Gillett, N. P., ... Sigmond, M. (2019a). *CCCma CanESM5-CanOE model output prepared for CMIP6 CMIP historical [Dataset]*. Earth System Grid Federation. doi: 10.22033/ESGF/CMIP6.10260
- Swart, N. C., Cole, J. N., Kharin, V. V., Lazare, M., Scinocca, J. F., Gillett, N. P.,

- ... Sigmond, M. (2019b). *CCCma CanESM5 model output prepared for CMIP6 CMIP historical [Dataset]*. Earth System Grid Federation. doi: 10.22033/ESGF/CMIP6.3610
- Takahashi, T., Olafsson, J., Goddard, J. G., Chipman, D. W., & Sutherland, S. C. (1993). Seasonal variation of  $\text{CO}_2$  and nutrients in the high-latitude surface oceans: A comparative study. *Global Biogeochemical Cycles*, 7(4), 843-878. Retrieved from <https://agupubs.onlinelibrary.wiley.com/doi/abs/10.1029/93GB02263> doi: <https://doi.org/10.1029/93GB02263>
- Takahashi, T., Sutherland, S. C., Sweeney, C., Poisson, A., Metzl, N., Tilbrook, B., ... Nojiri, Y. (2002). Global sea-air  $\text{CO}_2$  flux based on climatological surface ocean  $\text{pCO}_2$ , and seasonal biological and temperature effects. *Deep Sea Research Part II: Topical Studies in Oceanography*, 49(9), 1601-1622. (The Southern Ocean I: Climatic Changes in the Cycle of Carbon in the Southern Ocean) doi: [https://doi.org/10.1016/S0967-0645\(02\)00003-6](https://doi.org/10.1016/S0967-0645(02)00003-6)
- Takahashi, T., Sutherland, S. C., Wanninkhof, R., Sweeney, C., Feely, R. A., Chipman, D. W., ... de Baar, H. J. (2009). Climatological mean and decadal change in surface ocean  $\text{pCO}_2$ , and net sea-air  $\text{CO}_2$  flux over the global oceans. *Deep Sea Research Part II: Topical Studies in Oceanography*, 56(8), 554-577. Retrieved from <https://www.sciencedirect.com/science/article/pii/S0967064508004311> (Surface Ocean  $\text{CO}_2$  Variability and Vulnerabilities) doi: <https://doi.org/10.1016/j.dsr.2008.12.009>
- Taylor, K. E., Stouffer, R. J., & Meehl, G. A. (2012). An overview of cmip5 and the experiment design. *Bulletin of the American meteorological Society*, 93(4), 485-498.
- Vaithinada Ayar, P., Tjiputra, J., Bopp, L., Christian, J. R., Ilyina, T., Krasting, J. P., ... Yool, A. (2022). Contrasting projection of the enso-driven  $\text{CO}_2$  flux variability in the equatorial pacific under high warming scenario. *Earth System Dynamics Discussions*, 2022, 1-31. Retrieved from <https://esd.copernicus.org/preprints/esd-2022-12/> doi: 10.5194/esd-2022-12
- Wanninkhof, R. (2014). Relationship between wind speed and gas exchange over the ocean revisited. *Limnology and Oceanography: Methods*, 12(6), 351-362. Retrieved from <https://aslopubs.onlinelibrary.wiley.com/doi/abs/10.4319/lom.2014.12.351> doi: <https://doi.org/10.4319/lom.2014.12.351>
- Wieners, K.-H., Giorgetta, M., Jungclaus, J., Reick, C., Esch, M., Bittner, M., ... Roeckner, E. (2019). *MPI-M MPI-ESM1.2-LR model output prepared for CMIP6 CMIP historical [Dataset]*. Earth System Grid Federation. doi: 10.22033/ESGF/CMIP6.6595
- Yukimoto, S., Koshiro, T., Kawai, H., Oshima, N., Yoshida, K., Urakawa, S., ... Adachi, Y. (2019). *MRI MRI-ESM2.0 model output prepared for CMIP6 CMIP historical [Dataset]*. Earth System Grid Federation. doi: 10.22033/ESGF/CMIP6.6842
- Ziehn, T., Chamberlain, M., Lenton, A., Law, R., Bodman, R., Dix, M., ... Druken, K. (2019). *CSIRO ACCESS-ESM1.5 model output prepared for CMIP6 CMIP historical [Dataset]*. Earth System Grid Federation. doi: 10.22033/ESGF/CMIP6.4272
- Zuo, H., Balmaseda, M. A., Tietsche, S., Mogensen, K., & Mayer, M. (2019). The ecmwf operational ensemble reanalysis-analysis system for ocean and sea ice: a description of the system and assessment. *Ocean Science*, 15(3), 779-808. Retrieved from <https://os.copernicus.org/articles/15/779/2019/> doi: 10.5194/os-15-779-2019

# Supporting Information for "Equatorial Pacific pCO<sub>2</sub> Interannual Variability in CMIP6 Models"

Suki C. K. Wong<sup>1</sup>, Galen A. McKinley<sup>1</sup>, Richard Seager<sup>1</sup>

<sup>1</sup>Lamont-Doherty Earth Observatory, Columbia University, Palisades, New York

## Contents of this file

1. Tables S1 to S2
2. Figures S3 to S9

---

Corresponding author: Suki C. K. Wong, Lamont-Doherty Earth Observatory, Columbia University, Palisades, New York. (suki.wong@columbia.edu)



**Table S1.** The CMIP6 models and the ensemble members used in this assessment. The members in bold were the members used to represent the model whenever a single member was used in a calculation or plot.

Models	Member IDs
ACCESS-ESM1-5	<b>r1i1p1f1</b> , r2i1p1f1, r3i1p1f1, r4i1p1f1, r5i1p1f1, r6i1p1f1, r8i1p1f1
CanESM5	<b>r1i1p1f1</b> , r2i1p1f1, r3i1p1f1, r4i1p1f1, r5i1p1f1, r6i1p1f1, r7i1p1f1, r8i1p1f1, r9i1p1f1, r10i1p1f1, r11i1p1f1, r12i1p1f1, r13i1p1f1, r14i1p1f1, r15i1p1f1, r16i1p1f1, r17i1p1f1, r18i1p1f1, r19i1p1f1, r20i1p1f1, r21i1p1f1, r22i1p1f1, r23i1p1f1, r24i1p1f1, r25i1p1f1, r1i1p2f1, r2i1p2f1, r3i1p2f1, r4i1p2f1, r5i1p2f1, r6i1p2f1, r7i1p2f1, r8i1p2f1, r9i1p2f1, r10i1p2f1
CanESM5-CanOE	<b>r1i1p1f1</b> , r2i1p1f1, r3i1p1f1
CESM2	<b>r1i1p1f1</b> , r2i1p1f1, r3i1p1f1, r4i1p1f1, r5i1p1f1, r6i1p1f1, r7i1p1f1, r8i1p1f1, r9i1p1f1, r10i1p1f1
CESM2-FV2	<b>r1i1p1f1</b> , r2i1p1f1, r3i1p1f1
CESM2-WACCM	<b>r1i1p1f1</b> , r2i1p1f1, r3i1p1f1
CESM2-WACCM-FV2	<b>r1i1p1f1</b> , r2i1p1f1, r3i1p1f1
CNRM-ESM2-1	<b>r1i1p1f2</b> , r2i1p1f2, r3i1p1f2, r4i1p1f2, r5i1p1f2, r6i1p1f2, r7i1p1f2, r8i1p1f2, r9i1p1f2, r10i1p1f2, r11i1p1f2
GFDL-CM4	<b>r1i1p1f1</b>
IPSL-CM6A-LR	<b>r1i1p1f1</b> , r2i1p1f1, r3i1p1f1, r4i1p1f1, r5i1p1f1, r6i1p1f1, r7i1p1f1, r8i1p1f1, r9i1p1f1, r10i1p1f1, r11i1p1f1, r12i1p1f1, r13i1p1f1, r14i1p1f1, r15i1p1f1, r16i1p1f1, r17i1p1f1, r18i1p1f1, r19i1p1f1, r20i1p1f1, r21i1p1f1, r22i1p1f1, r23i1p1f1, r24i1p1f1, r25i1p1f1, r26i1p1f1, r27i1p1f1, r28i1p1f1, r29i1p1f1, r30i1p1f1, r31i1p1f1, r32i1p1f1
MIROC-ES2L	<b>r1i1p1f2</b> , r2i1p1f2, r3i1p1f2, r4i1p1f2, r5i1p1f2, r6i1p1f2, r7i1p1f2, r8i1p1f2, r9i1p1f2, r10i1p1f2
MRI-ESM2-0	<b>r1i2p1f1</b>
MPI-ESM1-2-LR	<b>r1i1p1f1</b> , r2i1p1f1, r3i1p1f1, r4i1p1f1, r5i1p1f1, r6i1p1f1, r7i1p1f1, r8i1p1f1, r9i1p1f1, r10i1p1f1
MPI-ESM1-2-HR	<b>r1i1p1f1</b> , r2i1p1f1, r3i1p1f1, r4i1p1f1, r5i1p1f1, r6i1p1f1, r7i1p1f1, r8i1p1f1, r9i1p1f1, r10i1p1f1
MPI-ESM1-2-HAM	<b>r1i1p1f1</b> , r2i1p1f1
NorESM2-LM	<b>r1i1p1f1</b> , r2i1p1f1, r3i1p1f1
NorESM2-MM	<b>r1i1p1f1</b> , r2i1p1f1, r3i1p1f1
UKESM1-0-LL	<b>r1i1p1f2</b> , r2i1p1f2, r3i1p1f2, r4i1p1f2, r5i1p1f3, r6i1p1f3, r7i1p1f3, r8i1p1f2, r9i1p1f2, r10i1p1f2, r11i1p1f2, r12i1p1f2, r16i1p1f2, r17i1p1f2, r18i1p1f2, r19i1p1f2

**Table S2.** One standard deviation of each Reynold's decomposition term relative to the time-tendency of pCO<sub>2,nonT</sub> in models. Values were calculated from a single member run from each model. \* The first row shows only the ratio for the second Reynold's term, calculated from a combination of the observations-based products (SeaFlux, ORAS5 and GLODAP). The last column shows the correlation coefficient (r) between  $w_{50}\partial_z DIC$  and pCO<sub>2,nonT</sub> variability.

Models*	$\frac{\sigma(w_{50}\partial_z DIC')}{\sigma(\partial_t pCO'_{2,nonT})}$	$\frac{\sigma(w'_{50}\partial_z \overline{DIC})}{\sigma(\partial_t pCO'_{2,nonT})}$	$\frac{\sigma(w'_{50}\partial_z DIC')}{\sigma(\partial_t pCO'_{2,nonT})}$	$\frac{\sigma(w_{50}\partial_z DIC)}{\sigma(\partial_t pCO'_{2,nonT})}$	r
obs-based products	-	4.04	-	-	-
CanESM5	1.91	2.50	1.22	3.51	0.51
CESM2	2.65	2.77	0.96	4.92	0.70
CESM2-FV2	2.08	1.99	0.92	3.72	0.66
CESM2-WACCM	2.67	2.94	0.87	4.91	0.67
CESM2-WACCM-FV2	1.87	2.55	0.82	3.82	0.58
CNRM-ESM2-1	2.03	2.30	1.01	3.59	0.47
GFDL-CM4	1.90	3.16	0.89	4.45	0.63
MIROC-ES2L	2.64	2.17	1.73	3.33	0.31
MRI-ESM2-0	1.96	2.26	0.95	3.79	0.51
NorESM2-LM	1.36	2.03	1.09	2.94	0.51
NorESM2-MM	2.06	2.30	1.26	3.38	0.51
UKESM1-0-LL	2.09	4.11	1.47	5.55	0.54

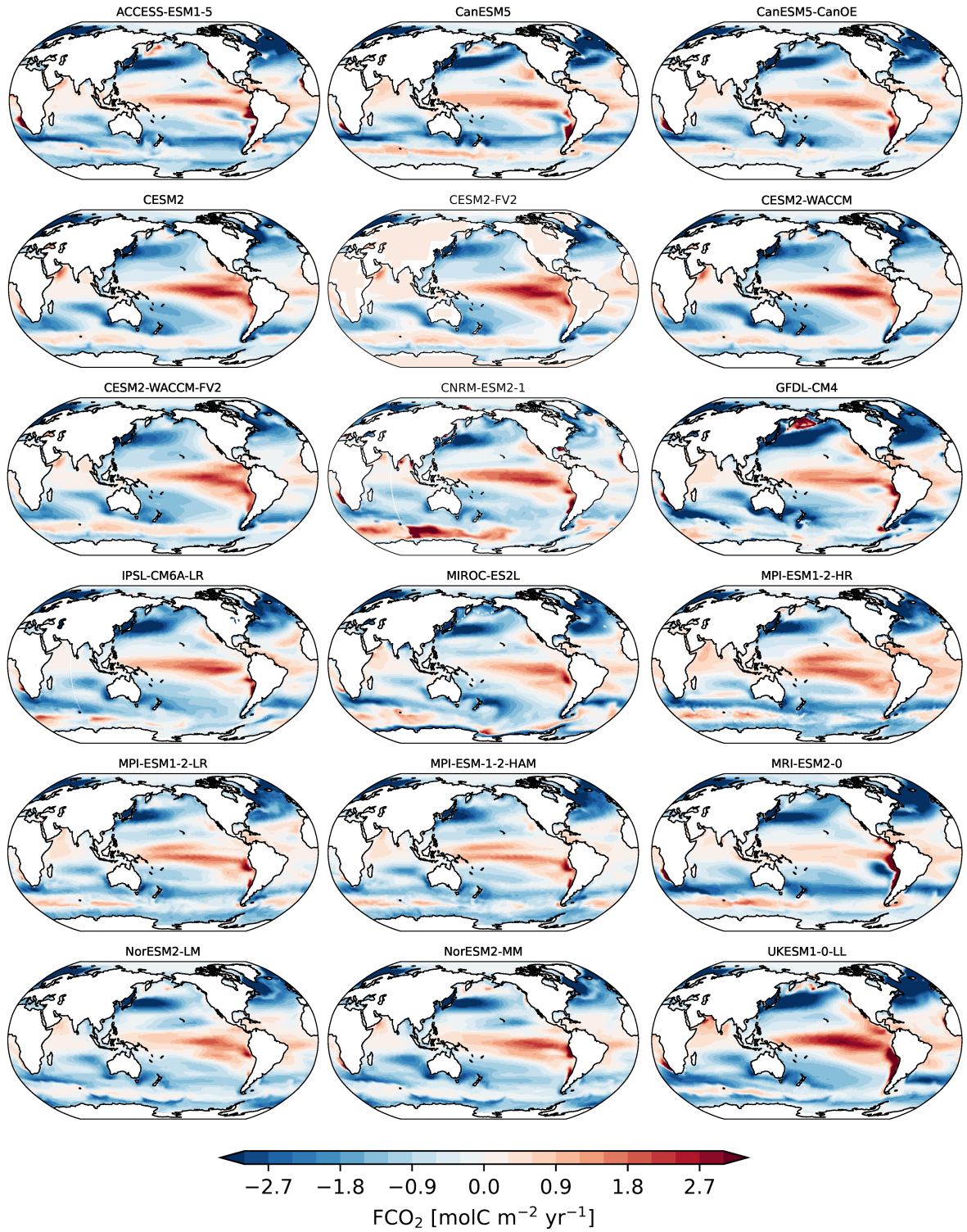


**Figure S1.** Multiyear mean maps of air-sea CO<sub>2</sub> flux (FCO<sub>2</sub> units: molC m<sup>-2</sup> yr<sup>-1</sup> taken over 1990-2014 for 18 CMIP6 models (one member was chosen per model). Positive values (red) represent fluxes from the ocean to the atmosphere.

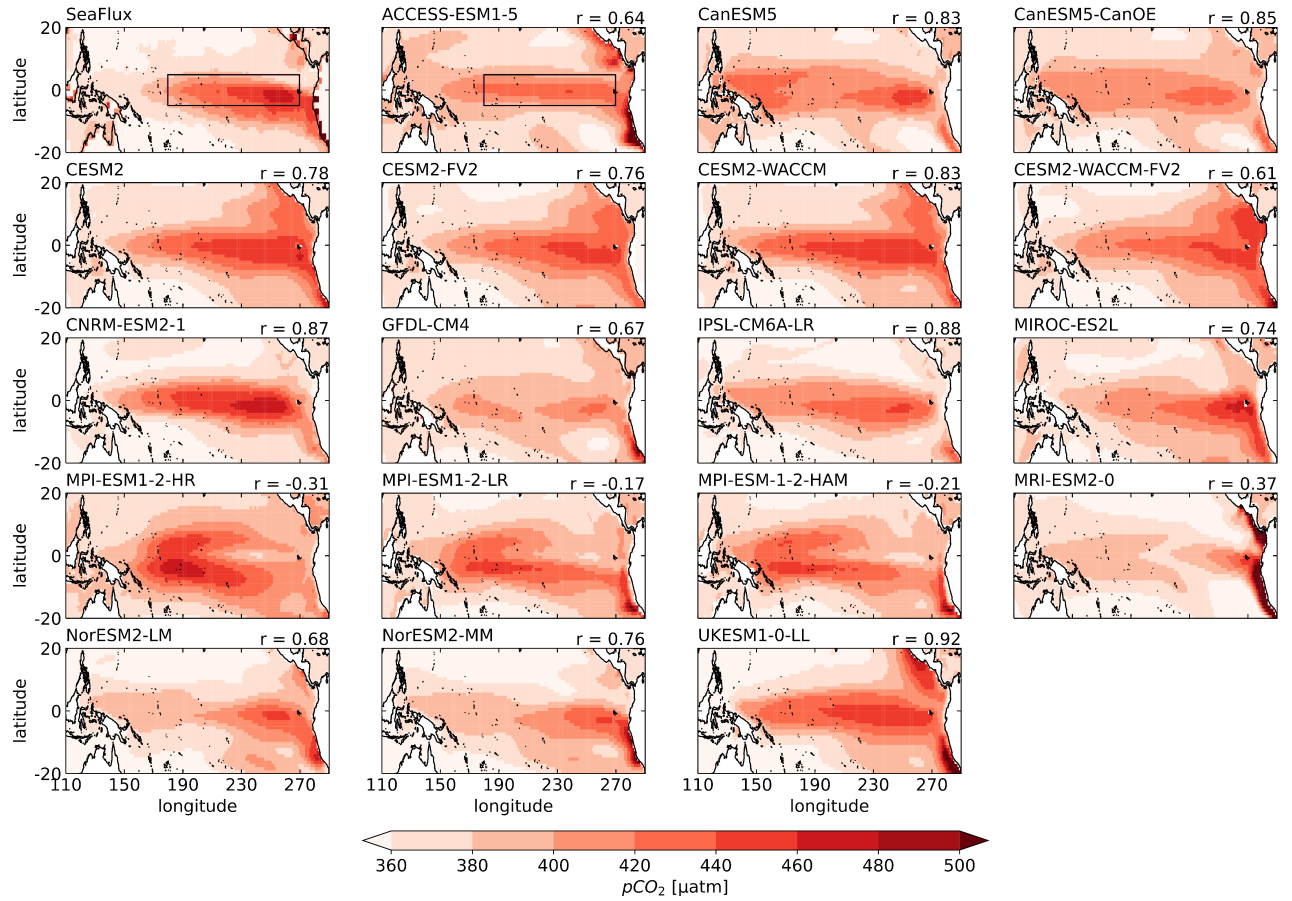


**Figure S2.** Tropical Pacific pCO<sub>2</sub> multi-year means from 1990-2014 (units:  $\mu\text{atm}$ ) from the SeaFlux ensemble average (top left) and 18 CMIP6 models (other panels). Boxes in the SeaFlux and ACCESS-ESM1-5 panels mark the TPI region. The number (r) on the top right of each model's map is the SCC between the model and SeaFlux in the TPI region. Model multi-year means are evaluated using a single ensemble member per model.

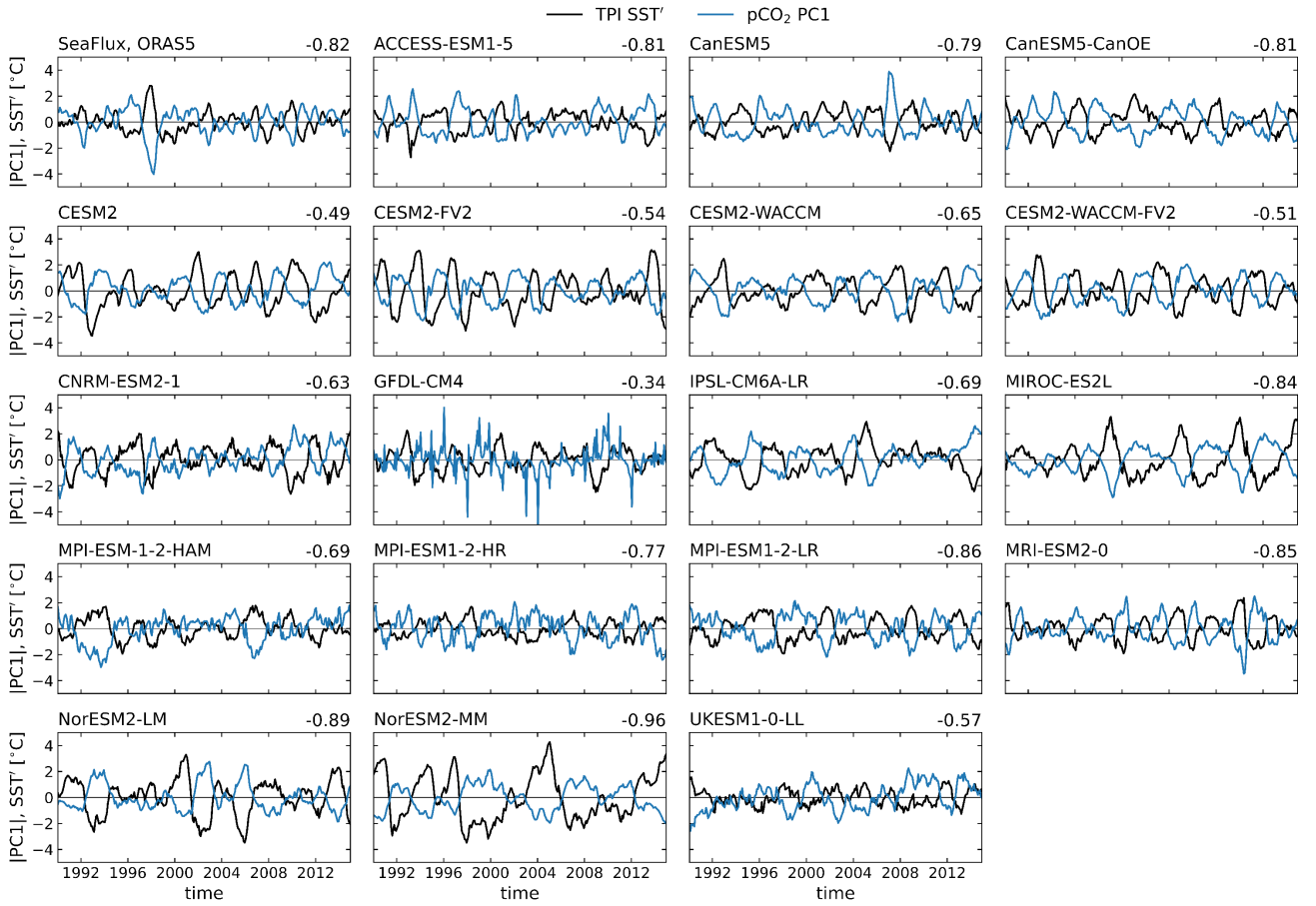


**Figure S3.** 1990-2014 time series of TPI SST anomalies (black lines) and the first principal component (PC1) of pCO<sub>2</sub> variability (blue lines) evaluated from ORAS5 and SeaFlux data, respectively (top-left). The other panels show the time series from 18 CMIP6 models. The correlation between TPI SST anomalies and pCO<sub>2</sub> PC1 are indicated by the number on the top-right of each panel.

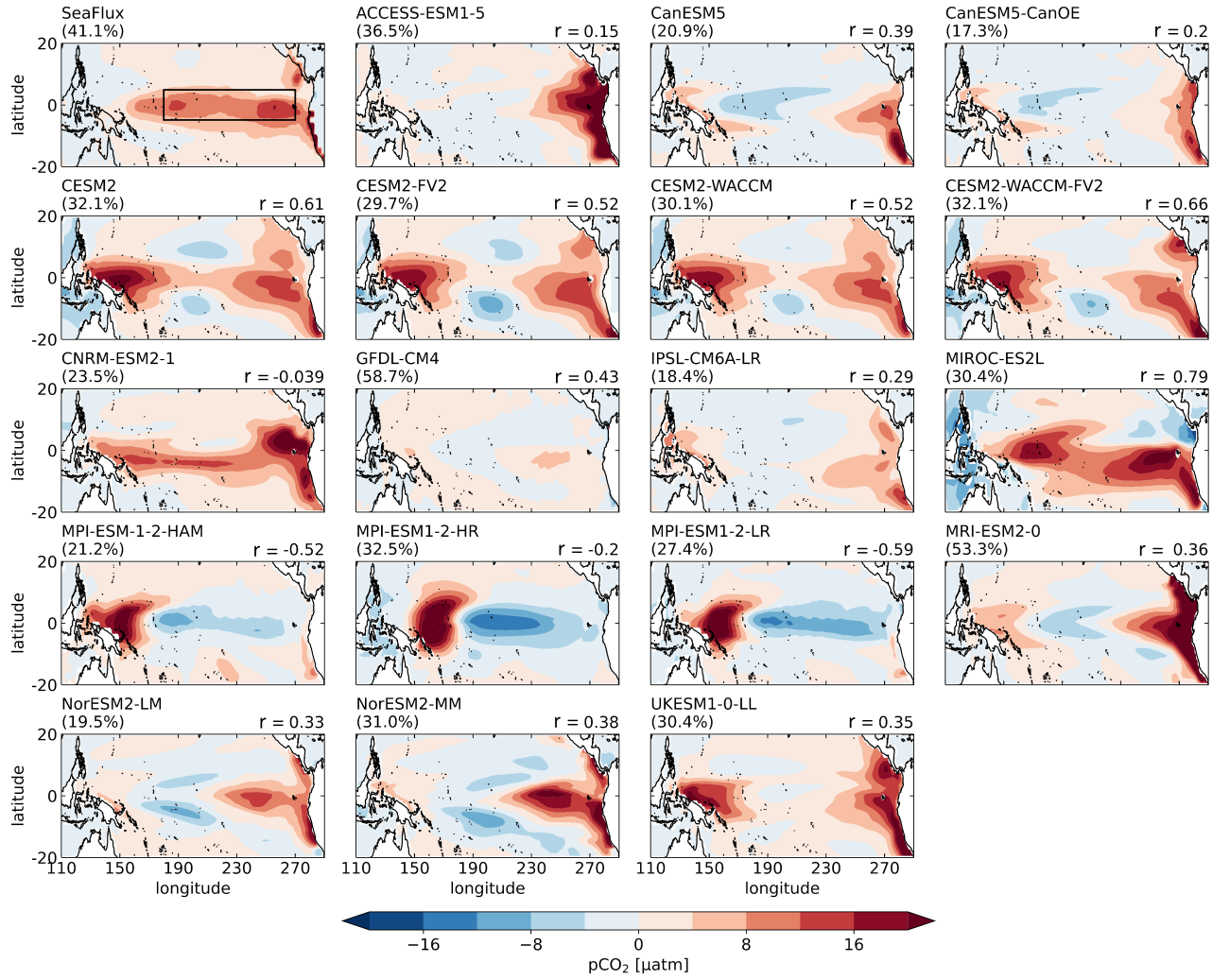


**Figure S4.** The first EOFs (units:  $\mu\text{atm}$ ) of detrended pCO<sub>2</sub> anomalies in SeaFlux, averaged across the ensemble (top left), and 18 CMIP6 models (other panels). Model EOF patterns are calculated individually for each ensemble member before averaging over the ensemble. The percentage of the total variance in the tropical Pacific explained by EOF1 is given in parentheses above each panel. The number ( $r$ ) on the top right of each model's panel is the SCC over the TPI region between each model's EOF1 and SeaFlux's EOF1. The TPI region is shown by the box in the top-left panel. The corresponding PC1 timeseries are shown in Figure S3.



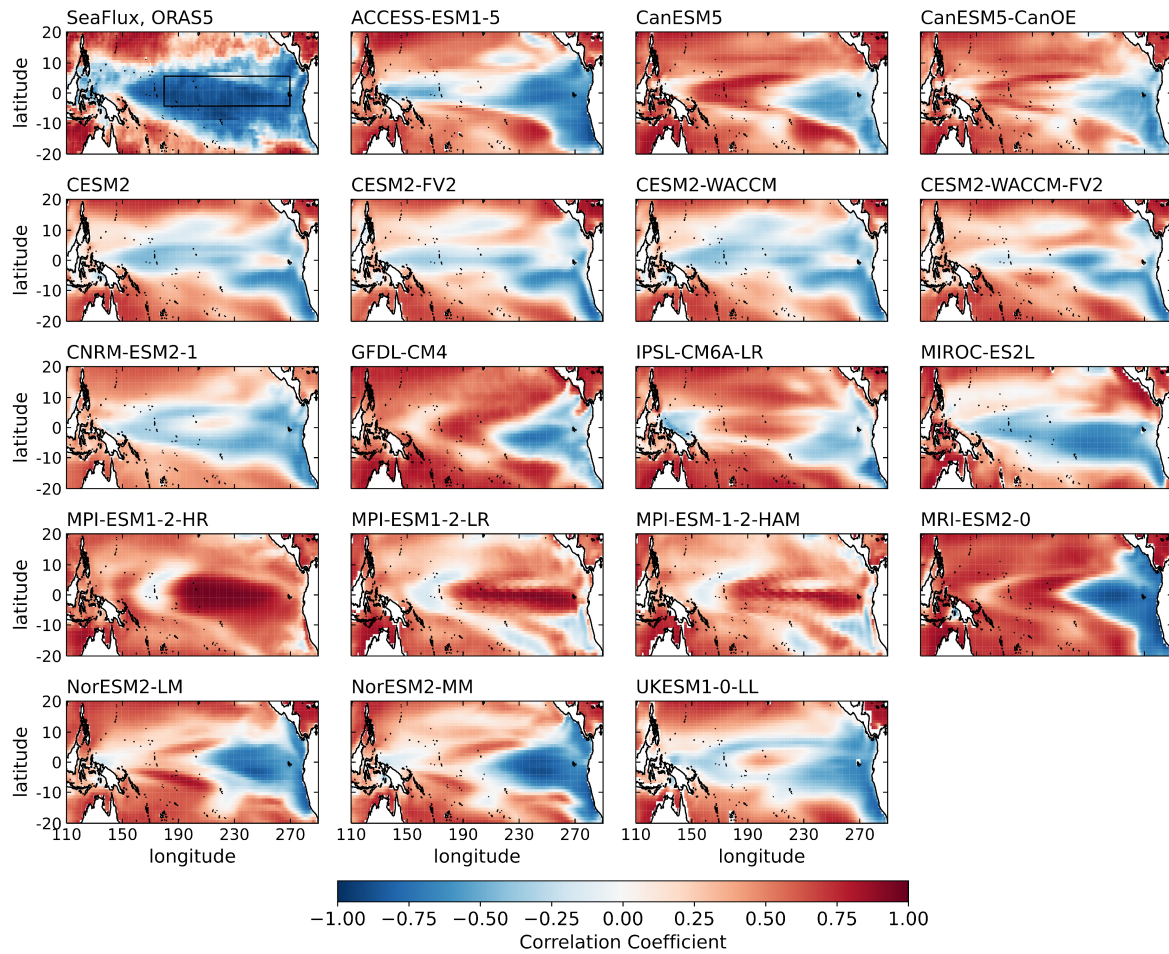


**Figure S5.** Correlation maps of detrended, pCO<sub>2</sub> and SST monthly anomalies over the tropical Pacific region. Time periods used: 1990-2014 for SeaFlux and ORAS5 (top-left), and 1959-2014 for models (other panels). Model correlation maps were calculated individually for each ensemble member before averaging over the ensemble. For the observations-based map, the mean across SeaFlux pCO<sub>2</sub> products was first taken before correlating with ORAS5 SSTs.

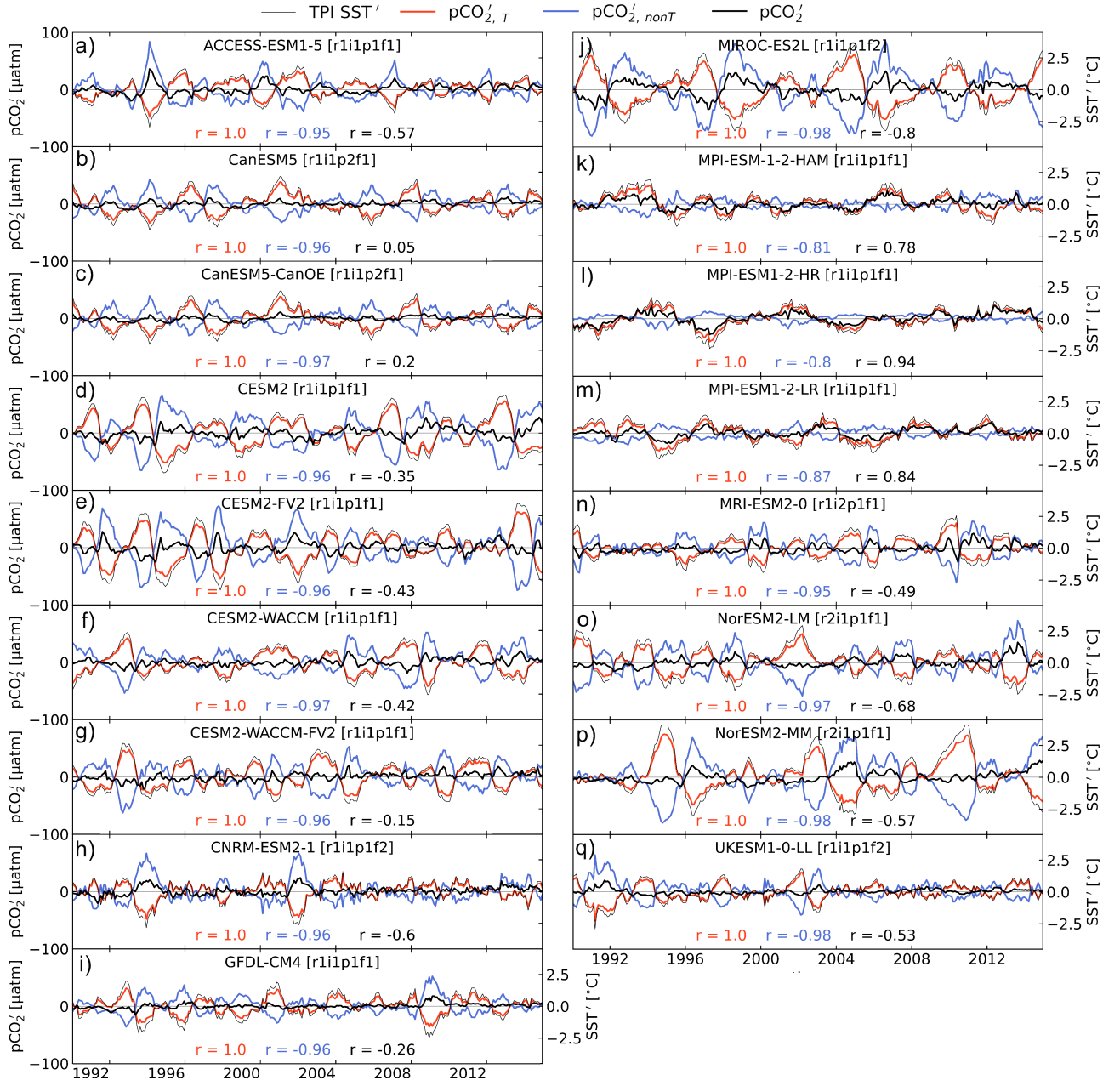


**Figure S6.** Thermal (red), non-thermal (blue), and total (bold black) pCO<sub>2</sub> anomalies (units:  $\mu\text{atm}$ ) and TPI SST anomalies (thin black; units:  $^{\circ}\text{C}$ ) over 1990-2014. Each panel (a through q) represents the time series from a single ensemble member from each CMIP6 model in this study. Correlation coefficients ( $r$ ) between pCO<sub>2,T</sub>, pCO<sub>2,nonT</sub> and total pCO<sub>2</sub> anomalies with TPI SST anomalies are shown in each panel in red, blue and black, respectively.



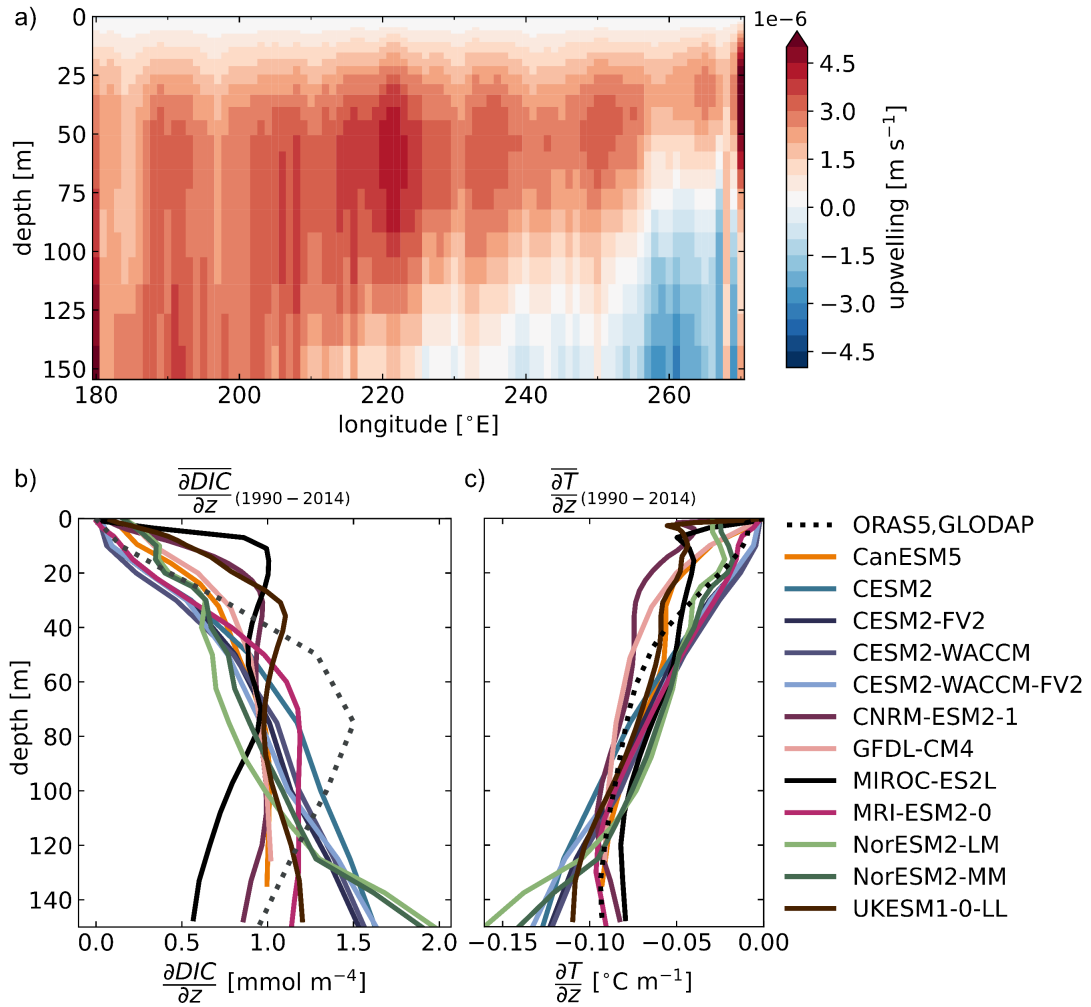


**Figure S7.** a) Time-averaged (1990-2014) upwelling section from ORAS5. The section was averaged between 5°N to 5°S. Positive values indicate upwelling (units: ms<sup>-1</sup>). b) Vertical gradients of climatological DIC (units: mmolm<sup>-4</sup>). GLODAPv2's DIC gradient is represented by the dashed black line. c) vertical gradients of climatological ocean temperatures (units: °Cm<sup>-1</sup>). ORAS5's temperature gradient is represented by the dashed black line.

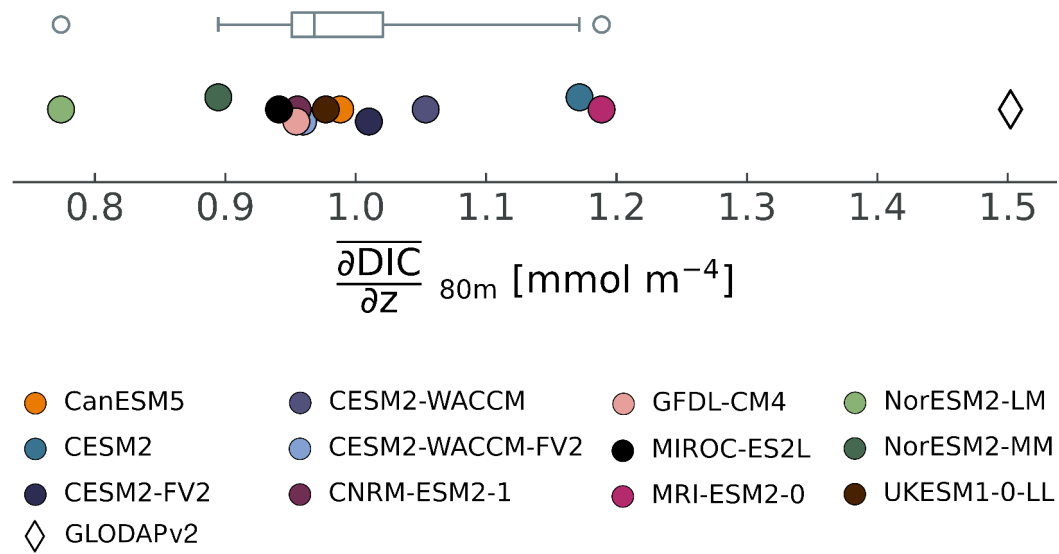


**Figure S8.** Amplitudes (units:  $\text{mmol m}^{-4}$ ) of vertical gradients of climatological DIC, evaluated at 80m depth, across CMIP6 models (filled circles) versus GLODAPv2 (clear diamond). The boxplot represents the CMIP6 models.

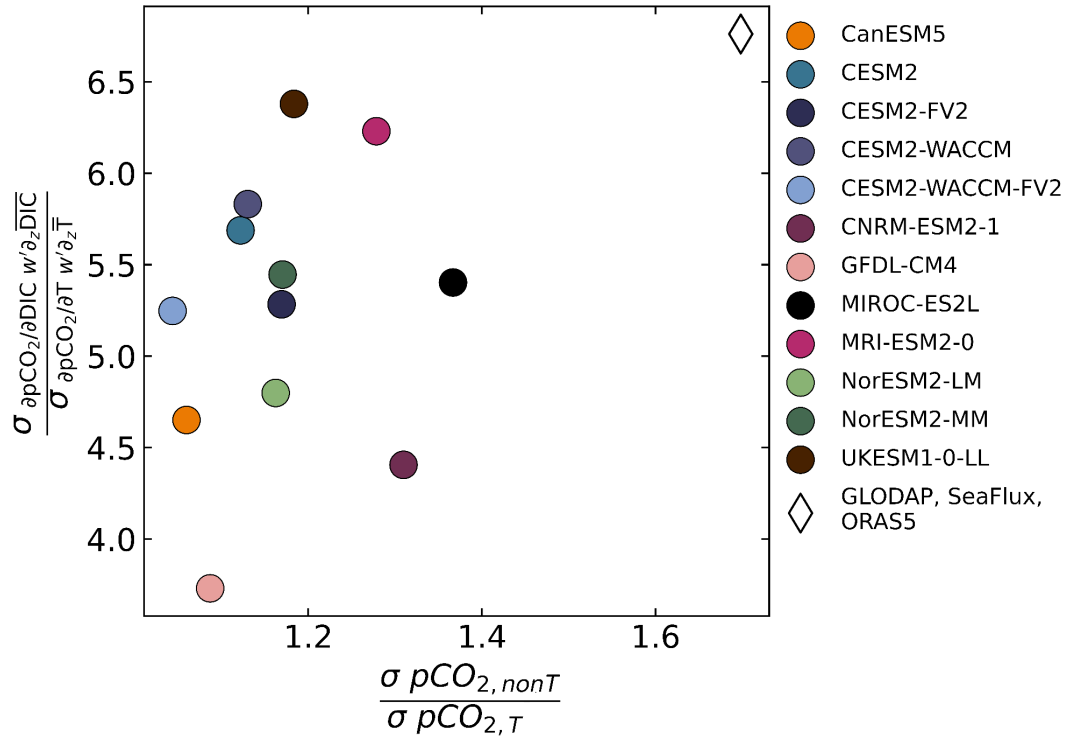


**Figure S9.** x-axis: Ratio of pCO<sub>2,nonT</sub> IAV to pCO<sub>2,T</sub> IAV (units: dimensionless). y-axis: Ratio of the vertical DIC gradients to the vertical temperature gradients at 50m depth, converted into units of pCO<sub>2</sub> tendency (ratio units: dimensionless). Models are marked by filled circles and the observations-based data are the marked by the clear diamond. Each model here is represented by one ensemble member.